Mesoscopic lattice Boltzmann modeling of dense gas flows in curvilinear geometries

Sergiu Busuioc [*]

Department of Physics, West University of Timioara, Bd. Vasile Pârvan 4, 300223 Timioara, Romania and Institute for Advanced Environmental Research, West University of Timioara, Bd. Vasile Pârvan 4, 300223 Timioara, Romania

(Received 22 March 2024; accepted 6 May 2024; published 23 May 2024)

The Enskog equation with respect to orthonormal vielbein fields is derived in this paper, enabling the utilization of arbitrary coordinate systems to characterize spatial geometry. Additionally, an adapted coordinate system in the momentum space is employed, connected to the physical space through vielbeins. Within this framework, the momentum component perpendicular to a curved boundary can be treated as an independent one, facilitating the application of half-range Gauss-Hermite quadratures. An appropriate finite-difference lattice Boltzmann model is developed and validated against a direct simulation Monte Carlo particle-based method for solving the Enskog equation in curvilinear geometries. The test scenarios include cylindrical Couette flow, cylindrical Fourier flow between coaxial cylinders, and spherical Fourier flow between concentric spheres. Reasonable agreement between the two approaches is observed throughout the parameter range and curvature-specific effects are well captured.

DOI: 10.1103/PhysRevFluids.9.053401

I. INTRODUCTION

Rarefied gas flows characterized by non-negligible Knudsen numbers (Kn), representing the ratio between the mean-free path of fluid molecules and the characteristic length of the flow domain, have traditionally been investigated numerically using the Boltzmann equation, treating fluid constituents as point particles. However, when the mean-free path becomes comparable to the particle size, the finite molecular size's influence becomes critical [1]. Practical applications involving this scenario are the single-bubble sonoluminescence [2], high-pressure shock tubes [3], flows through microfabricated nanomembranes [4], and the gas extraction in unconventional reservoirs [5,6]. The Enskog equation [7] provides a means to extend the kinetic theory description beyond the dilute-gas Boltzmann limit. Unlike the Boltzmann approach, the Enskog equation accounts for the finite size of gas molecules, incorporating space correlations between colliding molecules, molecular mutual shielding, and reduction of available volume [1,7–10]. Numerical solutions of the Enskog equation can be achieved through probabilistic or deterministic methodologies, mirroring the approaches used for the Boltzmann equation. Deterministic techniques, including the Monte Carlo quadrature method [11], the fast spectral method [5,12], and the Fokker-Planck approximation [13,14], have been applied to tackle the Enskog equation. On the other hand, probabilistic methods have emerged, inspired by the success of the direct simulation Monte Carlo (DSMC) method pioneered by Alexander *et al.* [15], Montanero *et al.* [16], and Frezzotti [17]. These methods have been applied to investigate dense gases near solid walls in microchannels and nanochannels [17–23]. Its extension to weakly attracting hard-sphere systems has demonstrated efficacy in characterizing

[*]sergiu.busuioc@e-uvt.ro

various phenomena, including monoatomic [24–27], polyatomic fluids [28,29], mixtures [30], the formation and rupture of liquid menisci in nanochannels [31], as well as the growth or collapse dynamics of spherical nanodroplets and bubbles [32]. Despite their reliability, these methods are computationally intensive. To address this, a common approach is to simplify the Enskog collision integral by expanding it into a Taylor series. This simplification, utilized in lattice Boltzmann (LB) models, has been successful in investigating nonideal gases [33–35] and multiphase flows [36]. More recently, the simplified Enskog collision operator has been successfully implemented in various solvers, including the discrete unified gas kinetic scheme (DUGKS) [37], the discrete velocity method (DVM) [23,38], the discrete Boltzmann method (DBM) [39,40], the double-distribution lattice Boltzmann model (DDLB) [41], and the finite-difference lattice Boltzmann (FDLB) models [42,43]. These solvers offer computationally efficient alternatives for investigating microscale flow phenomena while maintaining reasonable accuracy.

In this paper, the recently introduced finite-difference lattice Boltzmann (FDLB) model for bounded dense gas flows [43] is further extended to tackle flows in curvilinear geometries. In the literature, it is a common approach to leverage the symmetries inherent in non-Cartesian geometries through the use of curvilinear geometry-fitted coordinates [44–49]. These coordinates can be selected such that the boundary aligns orthogonally with the unit vector along one of the curvilinear axes. To ensure the implementation of the half-range quadratures [50,51] along the direction perpendicular to the boundary, an additional step is necessary: the momentum space must be adjusted to align with the new coordinate system, ensuring that the momentum vector components consistently align with the unit vectors corresponding to the curvilinear coordinates. In Ref. [52], the relativistic Boltzmann equation has been expressed in conservative form with respect to a vielbein (i.e., tetrad) field and a general choice for the parametrization of the momentum space. Later, in Ref. [51], a formulation of the Boltzmann equation with respect to general coordinates has been presented. In order to keep the momentum space tied to the new coordinate frame, an orthonormal vielbein field (i.e., triad consisting of the nonholonomic unit vectors of the coordinate frame) has been employed, with respect to which the momentum space degrees of freedom are defined. The resulting Boltzmann equation contains inertial forces that ensure that freely streaming particles travel along straight lines in the original Cartesian geometry. Following [51], the same vielbein framework is applied to the Enskog equation, in order to tackle the flow of dense gases in curvilinear geometries. This framework has been successfully applied to the torus geometry involving binary fluids [53].

Furthermore, the applicability of the proposed scheme to dense gas flows enclosed inside curved boundaries is demonstrated by considering the cylindrical Couette flow and cylindrical Fourier flow between coaxial cylinders, as well as the spherical Fourier flow between concentric spheres. In particular, the cylindrical and spherical coordinates are used to parametrize the flow domain, such that the boundaries are orthogonal to the radial directions R and r, for cylindrical and spherical coordinates systems, respectively. After expressing the momentum-space vectors with respect to the unit vectors, the mixed-quadrature lattice Boltzmann (LB) models introduced in Ref. [50] are employed. The mixed quadrature models allow the half-range or full-range Gauss-Hermite quadratures to be independently used on the coordinate axes of the momentum space. Quadrature methods generally result in off-lattice velocity sets where the number of vectors increases with the quadrature order, therefore, it is convenient to employ finite-difference methods. The implementation of the inertial forces requires the theory of distributions, as discussed in Refs. [51,54].

The structure of the paper is as follows. For the readers's convenience, in the first part of Sec. II, the simplified Enskog equation is presented along with the Shakhov collision term in Cartesian coordinates. The extension to general coordinates and the vielbein framework is discussed further as well as the cylindrical and spherical cases specific to the problems addressed in this study. The finite-difference lattice Boltzmann (FDLB) model with mixed quadratures used to numerically solve the simplified Enskog equation in cylindrically and spherically symmetric setups is briefly introduced in Sec. III. This model relies on half-range Gauss-Hermite quadratures in order to account for the boundary-induced discontinuities. The computer simulation results for the cylindrical Couette and

the Fourier flows between coaxial cylinders, as well as for the Fourier flow between concentric spheres, are reported in Sec. IV. The paper is concluded in Sec. V.

II. LATTICE BOLTZMANN MODEL IN CURVILINEAR GEOMETRIES

The Enskog equation, proposed in 1922 [7], describes the evolution of a system consisting of rigid spherical molecules. Unlike Boltzmann's equation, which assumes molecules as pointlike particles subjected to local collisions, Enskog's equation takes into account also the volume of the fluid molecules. This volume restricts the free movement space available to each particle, leading to an increased number of collisions. Additionally, the collisions between particles are nonlocal, occurring when the centers of the two colliding molecules are separated by one molecular diameter. The Enskog equation can be written as follows [8–10]:

$$\frac{\partial f}{\partial t}+\frac{\boldsymbol{p}}{m}\cdot\nabla_{\boldsymbol{x}}f+\boldsymbol{F}\cdot\nabla_{\boldsymbol{p}}f=J_E=\int\left\{\chi\left(\boldsymbol{x}+\frac{\sigma}{2}\boldsymbol{k}\right)f(\boldsymbol{x},\boldsymbol{p}^*)f(\boldsymbol{x}+\sigma\boldsymbol{k},\boldsymbol{p}_1^*)\right.$$
$$\left.-\chi\left(\boldsymbol{x}-\frac{\sigma}{2}\boldsymbol{k}\right)f(\boldsymbol{x},\boldsymbol{p})f(\boldsymbol{x}-\sigma\boldsymbol{k},\boldsymbol{p}_1)\right\}\sigma^2(\boldsymbol{p}_r\cdot\boldsymbol{k})d\boldsymbol{k}\,d\boldsymbol{p}_1, \tag{1}$$

where m denotes the particle mass, $\boldsymbol{F}=m\boldsymbol{a}$ represents the external body force, $f\equiv f(\boldsymbol{x},\boldsymbol{p},t)$ is the single-particle distribution function, σ represents the molecular diameter, $\boldsymbol{p}_r=\boldsymbol{p}_1-\boldsymbol{p}$ is the relative momentum, and $\boldsymbol{k}$ is the unit vector specifying the relative position of the two colliding particles. The time dependence of the distribution function is omitted for brevity. At time t, the distribution function f provides the number of particles located within the phase space volume $d\boldsymbol{x}\,d\boldsymbol{p}$ centered at the point $(\boldsymbol{x},\boldsymbol{p})$. The right-hand side of the equation above is the Enskog collision operator, denoted J_E.

The influence of the molecular diameter σ on the collision frequency is embedded within the contact value of the pair correlation function χ. In the standard Enskog theory (SET), $\chi\equiv\chi_{\mathrm{SET}}$ is assessed at the contact point of two colliding particles within a fluid assumed to be in uniform equilibrium [9]. An approximate yet precise expression for χ_{SET} reads as

$$\chi_{\mathrm{SET}}[n]=\frac{1}{nb}\left(\frac{P^{hs}}{nk_BT}-1\right)=\frac{1}{2}\frac{2-\eta}{(1-\eta)^3}, \tag{2}$$

which is derived from the equation of state (EOS) for the hard-sphere fluid proposed by Carnahan and Starling [55]. Here, n represents the particle-number density, $\eta=b\rho/4$ is the reduced particle density ($b=2\pi\sigma^3/3m$), P^{hs} is the pressure of the hard-sphere fluid, k_B is the Boltzmann constant, and T is the temperature. The square brackets in Eq. (2) indicate functional dependence.

In the revised Enskog theory (RET), the fluid is assumed to be in a nonuniform equilibrium state [9,10,56], leading to a position-dependent particle-number density. In this scenario, an effective approximation for the radial distribution function is obtained using the Fischer-Methfessel (FM) prescription [57]. This involves substituting the actual value of the particle-number density n in Eq. (2) with the average particle density $\overline{n}$ computed over a spherical volume of radius σ, centered at $\boldsymbol{x}-\frac{\sigma}{2}\boldsymbol{k}$:

$$\chi_{\mathrm{RET-FM}}\left[n\left(\boldsymbol{x}-\frac{\sigma}{2}\boldsymbol{k}\right)\right]=\chi_{\mathrm{SET}}\left[\overline{n}\left(\boldsymbol{x}-\frac{\sigma}{2}\boldsymbol{k}\right)\right]. \tag{3}$$

The average particle density $\overline{n}$ is defined as

$$\overline{n}(\boldsymbol{x})=\frac{3}{4\pi\sigma^3}\int_{\mathbb{R}^3}n(\boldsymbol{x}')w(\boldsymbol{x},\boldsymbol{x}')\,d\boldsymbol{x}',\quad w(\boldsymbol{x},\boldsymbol{x}')=\begin{cases}1, & \|\boldsymbol{x}'-\boldsymbol{x}\|<\sigma,\\ 0, & \|\boldsymbol{x}'-\boldsymbol{x}\|\geqslant\sigma.\end{cases} \tag{4}$$

The Enskog collision operator J_E can be viewed as an extension of the Boltzmann collision operator which accounts for particles with spatial extent. As the molecular diameter σ tends towards zero,

the contact value of the pair correlation function approaches unity ($\chi \to 1$), thereby recovering the Boltzmann collision operator [8,9].

Assuming that the pair correlation function χ and the distribution functions appearing in the Enskog collision integral J_E are smooth around the contact point $\boldsymbol{x}$, one can approximate these functions using a Taylor series expansion around $\boldsymbol{x}$, leading to the simplified Enskog collision operator $J_E \approx J_0 + J_1$ [8,9]:

$$J_0 \equiv J_0[f] = \chi \int (f^* f_1^* - f f_1)\sigma^2(\boldsymbol{p_r}\cdot\boldsymbol{k})d\boldsymbol{k}\, d\boldsymbol{p_1}, \tag{5}$$

$$J_1 \equiv J_1[f] = \chi\sigma \int \boldsymbol{k}(f^*\nabla f_1^* + f\nabla f_1)\sigma^2(\boldsymbol{p_r}\cdot\boldsymbol{k})d\boldsymbol{k}\, d\boldsymbol{p_1}$$
$$+\frac{\sigma}{2}\int \boldsymbol{k}\nabla\chi(f^* f_1^* + f f_1)\sigma^2(\boldsymbol{p_r}\cdot\boldsymbol{k})d\boldsymbol{k}\, d\boldsymbol{p_1}. \tag{6}$$

The term $J_0[f]$ corresponds to the conventional collision term of the Boltzmann equation multiplied by χ and is treated as such by applying the relaxation time approximation. In this study, the Shakhov collision term is employed [58,59]:

$$J_0[f] = -\frac{1}{\tau}(f - f^S), \tag{7}$$

where τ represents the relaxation time and f^S is the equilibrium Maxwell-Boltzmann distribution multiplied by a correction factor [58–61]:

$$f^S = f^{\mathrm{MB}}\left[1 + \frac{1-\mathrm{Pr}}{P_i k_B T}\left(\frac{\boldsymbol{\xi}^2}{5mk_BT} - 1\right)\boldsymbol{\xi}\cdot\boldsymbol{q}\right]. \tag{8}$$

The Maxwell-Boltzmann distribution f^{MB} is defined as

$$f^{\mathrm{MB}} = \frac{n}{(2m\pi k_B T)^{3/2}}\exp\left(-\frac{\boldsymbol{\xi}^2}{2mk_BT}\right), \tag{9}$$

and the heat flux $\boldsymbol{q}$ is obtained using $\boldsymbol{q} = \int d^3p\, f \frac{\boldsymbol{\xi}^2}{2m}\frac{\boldsymbol{\xi}}{m}$, where $\boldsymbol{\xi} = \boldsymbol{p} - m\boldsymbol{u}$ represents the peculiar momentum, $\mathrm{Pr} = c_P\mu/\lambda$ denotes the Prandtl number, $c_P = 5k_B/2m$ is the specific heat at constant pressure, μ is the shear viscosity, λ is the thermal conductivity, and $P_i = \rho\mathcal{G}T = nk_BT$ is the ideal gas equation of state, with $\mathcal{G}$ being the specific gas constant. It is important to note that although the Shakhov model does not guarantee the non-negativity of the correction factor and the H-theorem has not been proven, the model has been successfully implemented and its accuracy has been tested through comparisons with experimental [60,62,63] or DSMC [61,64–66] results.

The term $J_1[f]$ can be approximated by replacing the distribution functions (f^*, f_1^*, f, f_1) with their corresponding equilibrium distribution functions and integrating over $\boldsymbol{k}$ and $\boldsymbol{p_1}$ to obtain [8,9]

$$J_1[f] \approx J_1[f^{\mathrm{MB}}] = -b\rho\chi f^{\mathrm{MB}}\left\{\boldsymbol{\xi}\cdot\left[\nabla\ln(\rho^2\chi T) + \frac{3}{5}\left(\zeta^2 - \frac{5}{2}\right)\nabla\ln T\right]\right.$$
$$\left.+\frac{2}{5}\left[2\boldsymbol{\zeta}\boldsymbol{\zeta}:\nabla\boldsymbol{u} + \left(\zeta^2 - \frac{5}{2}\right)\nabla\cdot\boldsymbol{u}\right]\right\}, \tag{10}$$

where $\boldsymbol{\zeta} = \boldsymbol{\xi}/\sqrt{2RT}$. Incorporating these approximations, the Enskog equation (1) can be expressed as

$$\frac{\partial f}{\partial t} + \frac{\boldsymbol{p}}{m}\nabla\boldsymbol{x} f + \boldsymbol{F}\cdot\nabla_{\boldsymbol{p}} f = -\frac{1}{\tau}(f - f^S) + J_1[f^{\mathrm{MB}}]. \tag{11}$$

A. Enskog equation in curvilinear coordinates

In certain situations, it is convenient to introduce a set of arbitrary coordinates $\{x^{\tilde{1}}, x^{\tilde{2}}, x^{\tilde{3}}\}$, where $x^{\tilde{\imath}} \equiv x^{\tilde{\imath}}(x, y, z)$ (in this paper, the analysis is restricted to time-independent coordinate transformations). This coordinate transformation induces a metric $g_{\tilde{\imath}\tilde{\jmath}}$, as follows:

$$ds^2 = \delta_{ij} dx^i dx^j = dx^2 + dy^2 + dz^2 = g_{\tilde{\imath}\tilde{\jmath}} dx^{\tilde{\imath}} dx^{\tilde{\jmath}}, \tag{12}$$

such that

$$g_{\tilde{\imath}\tilde{\jmath}} = \delta_{ij} \frac{\partial x^i}{\partial x^{\tilde{\imath}}} \frac{\partial x^j}{\partial x^{\tilde{\jmath}}}. \tag{13}$$

The Enskog equation (1) can be written with respect to these new coordinates as follows:

$$\frac{\partial f}{\partial t} + \frac{p^{\tilde{\imath}}}{m} \frac{\partial f}{\partial x^{\tilde{\imath}}} + \left(F^{\tilde{\imath}} - \frac{1}{m} \Gamma^{\tilde{\imath}}_{\tilde{\jmath}\tilde{k}} p^{\tilde{\jmath}} p^{\tilde{k}} \right) \frac{\partial f}{\partial p^{\tilde{\imath}}} = J_E[f], \tag{14}$$

where the components $p^{\tilde{\imath}}$ and $F^{\tilde{\imath}}$ (with respect to the new coordinates) are related to the components p^i and F^i (expressed with respect to the old coordinates) through $p^{\tilde{\imath}} = \frac{\partial x^{\tilde{\imath}}}{\partial x^i} p^i$, $\quad F^{\tilde{\imath}} = \frac{\partial x^{\tilde{\imath}}}{\partial x^i} F^i$. The Christoffel symbols $\Gamma^{\tilde{\imath}}_{\tilde{\jmath}\tilde{k}}$ appearing in Eq. (14) are defined as

$$\Gamma^{\tilde{\imath}}_{\tilde{\jmath}\tilde{k}} = \frac{\partial x^{\tilde{\imath}}}{\partial x^\ell} \frac{\partial^2 x^\ell}{\partial x^{\tilde{\jmath}} \partial x^{\tilde{k}}} = \frac{1}{2} g^{\tilde{\imath}\tilde{\ell}} \left(\partial_{\tilde{k}} g_{\tilde{\ell}\tilde{\jmath}} + \partial_{\tilde{\jmath}} g_{\tilde{\ell}\tilde{k}} - \partial_{\tilde{\ell}} g_{\tilde{\jmath}\tilde{k}} \right).$$

The above formalism is sufficient to adapt the coordinate system to a curved boundary. However, the transition to an LB model is not straightforward since the momentum space has an intrinsic dependence on the coordinates. Indeed, the Maxwellian distribution f^{MB} (9) expressed with respect to the new coordinates reads as

$$f^{\mathrm{MB}} = \frac{n}{(2\pi m T)^{\frac{3}{2}}} \exp\left[-\frac{g_{\tilde{\imath}\tilde{\jmath}} (p^{\tilde{\imath}} - m u^{\tilde{\imath}})(p^{\tilde{\jmath}} - m u^{\tilde{\jmath}})}{2mT} \right], \tag{15}$$

while its moments are calculated as

$$M^{\tilde{\imath}_1, \ldots, \tilde{\imath}_n}_{\mathrm{MB}} = \sqrt{g} \int d^3\tilde{p}\, f^{\mathrm{MB}} p^{\tilde{\imath}_1} \ldots p^{\tilde{\imath}_n}, \tag{16}$$

where g is the determinant of the metric tensor $g_{\tilde{\imath}\tilde{\jmath}}$.

In order to eliminate the burden of this metric dependence in the expression for the Maxwellian, it is convenient to introduce a triad (vielbein) with respect to which the metric is diagonal [51]:

$$g_{\tilde{\imath}\tilde{\jmath}} dx^{\tilde{\imath}} dx^{\tilde{\jmath}} = \delta_{\hat{a}\hat{b}} \omega^{\hat{a}} \omega^{\hat{b}}, \quad \omega^{\hat{a}} = \omega^{\hat{a}}_{\tilde{\jmath}} dx^{\tilde{\jmath}}, \tag{17}$$

where $\omega^{\hat{a}}$ are the triad one-forms and it follows that

$$g_{\tilde{\imath}\tilde{\jmath}} = \delta_{\hat{a}\hat{b}} \omega^{\hat{a}}_{\tilde{\imath}} \omega^{\hat{b}}_{\tilde{\jmath}}. \tag{18}$$

The above equation allows three degrees of freedom for the system $\{\omega^{\hat{a}}_{\tilde{\jmath}}\}$, corresponding to the invariance of the right-hand side of Eq. (18) under rotations with respect to the hatted indices. It is possible to define triad vectors dual to the above one-forms by introducing the following inner product [51]:

$$\langle \omega^{\hat{b}}, e_{\hat{a}} \rangle \equiv e^{\tilde{\imath}}_{\hat{a}} \omega^{\hat{b}}_{\tilde{\imath}} = \delta^{\hat{b}}{}_{\hat{a}}, \quad \text{where} \quad e_{\hat{a}} = e^{\tilde{\imath}}_{\hat{a}} \frac{\partial}{\partial x^{\tilde{\imath}}}. \tag{19}$$

Using the above triad, the components of vectors can be expressed as $p^{\hat{a}} = \omega^{\hat{a}}_{\tilde{i}} p^{\tilde{i}}$, such that $g_{\tilde{i}\tilde{j}} p^{\tilde{i}} p^{\tilde{j}} = \delta_{\hat{a}\hat{b}} p^{\hat{a}} p^{\hat{b}}$, resulting in the following Maxwellian:

$$f^{\mathrm{MB}} = \frac{n}{(2\pi m T)^{\frac{3}{2}}} \exp\left[-\frac{\delta_{\hat{a}\hat{b}}(p^{\hat{a}} - m u^{\hat{a}})(p^{\hat{b}} - m u^{\hat{b}})}{2mT} \right], \tag{20}$$

where the metric dependence disappeared. Its moments can be written as

$$M^{\hat{a}_1,\ldots,\hat{a}_s}_{\mathrm{MB}} = \int d^3\hat{p}\, f^{\mathrm{MB}} p^{\hat{a}_1} \ldots p^{\hat{a}_s}. \tag{21}$$

Also, the moments of the distribution function f are given by

$$M^{\hat{a}_1,\ldots,\hat{a}_s} = \int d^3\hat{p}\, f\, p^{\hat{a}_1} \ldots p^{\hat{a}_s}. \tag{22}$$

In curvilinear coordinates, the Enskog equation reads as

$$\begin{aligned} &\frac{\partial f}{\partial t} + \frac{p^{\hat{a}}}{m} e^{\tilde{i}}_{\hat{a}} \frac{\partial f}{\partial x^{\tilde{i}}} + \left(F^{\hat{a}} - \frac{1}{m} \Gamma^{\hat{a}}{}_{\hat{b}\hat{c}} p^{\hat{b}} p^{\hat{c}} \right) \frac{\partial f}{\partial p^{\hat{a}}} \\ &\quad = -\frac{1}{\tau}(f - f^S) - b\rho\chi f^{\mathrm{MB}} \left\{ \xi^{\hat{a}} \cdot \left[\nabla_{\hat{a}} \ln(\rho^2 \chi T) + \frac{3}{5}\left(\zeta^2 - \frac{5}{2} \right) \nabla_{\hat{a}} \ln T \right] \right. \\ &\qquad \left. + \frac{2}{5}\left[2\zeta^{\hat{a}}\zeta^{\hat{b}} : \nabla_{\hat{a}} u^{\hat{b}} + \left(\zeta^2 - \frac{5}{2} \right) \nabla_{\hat{a}} \cdot u^{\hat{a}} \right] \right\}, \end{aligned} \tag{23}$$

where $\zeta^{\hat{a}} = \xi^{\hat{a}}/\sqrt{2RT}$. In the above, the Enskog collision operator is replaced with the simplified Enskog collision operator.

The relations between the distribution function f and the particle-number density n, macroscopic velocity $u^{\hat{a}}$, stress tensor $T^{\hat{a}\hat{b}}$, and heat flux $q^{\hat{a}}$ are listed below:

$$n = \int d^3\hat{p}\, f, \qquad u^{\hat{a}} = \frac{1}{\rho} \int d^3\hat{p}\, f\, p^{\hat{a}}, \tag{24a}$$

$$T^{\hat{a}\hat{b}} = \int d^3\hat{p}\, f\, \frac{\xi^{\hat{a}}\xi^{\hat{b}}}{m}, \qquad q^{\hat{a}} = \int d^3\hat{p}\, f\, \frac{\boldsymbol{\xi}^2}{2m} \frac{\xi^{\hat{a}}}{m}, \tag{24b}$$

where $\rho = mn$, $\xi^{\hat{a}} = p^{\hat{a}} - m u^{\hat{a}}$, $\boldsymbol{\xi}^2 = \delta_{\hat{a}\hat{b}} \xi^{\hat{a}} \xi^{\hat{b}}$, and the internal energy is $e = \frac{1}{2n} T^{\hat{a}}{}_{\hat{a}}$. The macroscopic fluid equations are

$$\frac{Dn}{Dt} + n(\nabla \cdot \boldsymbol{u}) = 0, \quad \rho \frac{D u^{\hat{a}}}{Dt} = n F^{\hat{a}} - \nabla_{\hat{b}} T^{\hat{a}\hat{b}}, \tag{25a}$$

$$n \frac{De}{Dt} + \nabla_{\hat{a}} q^{\hat{a}} + T^{\hat{a}\hat{b}} \nabla_{\hat{a}} u_{\hat{b}} = 0, \tag{25b}$$

where $D/Dt = \partial_t + u^{\hat{a}} \nabla_{\hat{a}}$ is the material derivative, while $e = \frac{3}{2} T$ is the internal energy. The heat flux $q^{\hat{a}}$ and the stress tensor $T^{\hat{a}\hat{b}}$ are given by

$$q^{\hat{a}} = -\lambda \nabla^{\hat{a}} T, \tag{26}$$

$$T^{\hat{a}\hat{b}} = \delta^{\hat{a}\hat{b}} P - \mu \left(\nabla^{\hat{a}} u^{\hat{b}} + \nabla^{\hat{b}} u^{\hat{a}} - \frac{2}{3} \delta^{\hat{a}\hat{b}} \nabla_{\hat{c}} u^{\hat{c}} \right), \tag{27}$$

where $P = P_i(1 + b\rho\chi)$ is the equation of thermodynamic pressure of a gas in uniform equilibrium.

The thermal conductivity λ and the shear viscosity μ, which appear in Eqs. (26), are given by [9]

$$\mu = \tau P_i = \mu_0 \left[\frac{1}{\chi} + \frac{4}{5}(b\rho) + \frac{4}{25}\left(1 + \frac{12}{\pi}\right)(b\rho)^2 \chi \right], \tag{28}$$

$$\lambda = \frac{5k_B}{2m}\frac{\tau P_i}{\mathrm{Pr}} = \lambda_0 \left[\frac{1}{\chi} + \frac{6}{5}(b\rho) + \frac{9}{25}\left(1 + \frac{32}{9\pi}\right)(b\rho)^2 \chi \right]. \tag{29}$$

In these equations, $\mu_0 = \frac{5}{16\sigma^2}\sqrt{\frac{mk_BT}{\pi}}$ and $\lambda_0 = \frac{75k_B}{64m\sigma^2}\sqrt{\frac{mk_BT}{\pi}}$ represent the viscosity coefficient and the thermal conductivity for an ideal gas of hard-sphere molecules at temperature T. For a dense gas, the Prandtl number Pr is expressed as [9]

$$\mathrm{Pr} = \frac{2}{3}\frac{1 + \frac{4}{5}b\rho\chi + \frac{4}{25}\left(1 + \frac{12}{\pi}\right)(b\rho\chi)^2}{1 + \frac{6}{5}b\rho\chi + \frac{9}{25}\left(1 + \frac{32}{9\pi}\right)(b\rho\chi)^2}. \tag{30}$$

The dilute limit $\sigma \to 0$ corresponds to $\mathrm{Pr} = \frac{2}{3}$. The Chapman-Enskog expansion of Eq. (23) provides relationships between the relaxation time τ and the transport coefficients. In this context, the relaxation time τ is expressed as

$$\tau = \frac{\mu}{P_i}. \tag{31}$$

The quantity μ encompasses both kinetic and potential contributions, which account for the flow of molecules and the collisional effects on the transfer of momentum and energy in the gas [8,9]. The relaxation time approximation effectively captures the collisional transfer resulting from nonlocal molecular collisions. It is worth noting that the viscosity of a dense gas with a fixed reduced density η can be adjusted by varying the molecular diameter σ and the number density n.

The Knudsen number is defined as the ratio of the mean-free path and a characteristic length (i.e., the distance between cylinders and spheres):

$$\mathrm{Kn} = \frac{\lambda}{L} = \frac{1}{6\sqrt{2}\eta_0\chi(\eta_0)C}, \tag{32}$$

where $C = L/\sigma$ is the confinement ratio [12,22,23].

This paper primarily concentrates on benchmarking the cylindrical Couette flow, as well as the cylindrical and spherical Fourier flow. In these cases, the steady flow either lacks bulk motion or exhibits motion perpendicular to the direction in which the gas density varies. Consequently, the bulk viscosity does not have an impact in these cases.

The model equation, incorporating the simplified Enskog collision operator J_1 [Eq. (10)], is constructed utilizing a limited set of low-order derivatives. This approach leads to the exclusion of higher-order terms, thereby sacrificing certain details of the system's behavior. However, this omission of high-order information in J_1, which does not appear in the momentum and energy transfer during collisions, is reintroduced in the kinetic transfer of momentum and energy through the relaxation time (31) and the Prandtl number (30) in the collision term $J_0[f]$ (7). Consequently, the resultant stress tensor and heat flux from the current kinetic model align with those derived from the Enskog equation. It is worth noting that the bulk viscosity term, absent in this formulation, can be reinstated by incorporating a second-order term in the Taylor expansion of the Enskog collision integral, as outlined in Refs. [23,67]. Hence, for the scope of this study, the focus is on flows where the bulk viscosity does not play a role. Consequently, when comparing heat fluxes obtained in the cylindrically and spherically symmetric Fourier flow, the simulation results using the PM will contain the total heat flux, both kinetic and potential contributions as defined in Ref. [20].

B. Cylindrical coordinates

Let us specialize the formalism of Sec. II A to the case of the Couette and Fourier flow between coaxial cylinders. To describe the geometry of this flow, it is convenient to introduce cylindrical

coordinates $\{\tilde{x^i}\} = \{R, \varphi, z\}$ through $x = R\cos\varphi$ and $y = R\sin\varphi$. The line element in cylindrical coordinates and the associated triad are

$$ds^2 = dR^2 + R^2 d\varphi^2 + dz^2, \qquad e_{\hat{R}} = \partial_R, \qquad e_{\hat{\varphi}} = R^{-1}\partial_\varphi, \qquad e_{\hat{z}} = \partial_z. \tag{33}$$

The nonvanishing connection coefficients for the triad (33) are

$$\Gamma^{\hat{R}}{}_{\hat{\varphi}\hat{\varphi}} = -\frac{1}{R}, \qquad \Gamma^{\hat{\varphi}}{}_{\hat{R}\hat{\varphi}} = \frac{1}{R}. \tag{34}$$

The Enskog equation when the flow is homogeneous with respect to φ and z reads as

$$\begin{aligned}
&\frac{\partial f}{\partial t} + \frac{2p^{\hat{R}}}{m}\frac{\partial(fR)}{\partial R^2} + \frac{1}{mR}\left[(p^{\hat{\varphi}})^2\frac{\partial f}{\partial p^{\hat{R}}} - p^{\hat{R}}\frac{\partial(fp^{\hat{\varphi}})}{\partial p^{\hat{\varphi}}}\right] \\
&\quad = \frac{1}{\tau}(f - f^S) - b\rho\chi f^{\mathrm{MB}}\left\{\xi^R\left[\partial_R \ln(\rho^2\chi T) + \frac{3}{5}\left(\zeta^2 - \frac{5}{2}\right)\partial_R \ln T\right]\right. \\
&\qquad \left. + \frac{2}{5}\left[2\zeta^{\hat{a}}\zeta^{\hat{b}} : \nabla_{\hat{a}}u^{\hat{b}} + \left(\zeta^2 - \frac{5}{2}\right)\partial_R u^R\right]\right\}.
\end{aligned} \tag{35}$$

The advection term is implemented following Ref. [68].

C. Spherical coordinates

To describe the spherical Fourier flow, the spherical coordinates $\{\tilde{x^i}\} = \{r, \theta, \varphi\}$ are introduced through $x = r\sin\theta\,\cos\varphi$, $y = r\,\sin\theta\,\sin\varphi$ and $z = r\,\cos\theta$. The line element in spherical coordinates and its associated triad are

$$ds^2 = dr^2 + r^2(d\theta^2 + \sin^2\theta\, d\varphi^2), \qquad e_{\hat{r}} = \partial_r, \qquad e_{\hat{\theta}} = \frac{\partial_\theta}{r}, \qquad e_{\hat{\varphi}} = \frac{r^{-1}}{\sin\theta}\partial_\varphi. \tag{36}$$

For this triad the nonvanishing connection coefficients are

$$\Gamma^{\hat{r}}{}_{\hat{\theta}\hat{\theta}} = -\Gamma^{\hat{\theta}}{}_{\hat{r}\hat{\theta}} = -\frac{1}{r}, \qquad \Gamma^{\hat{r}}{}_{\hat{\varphi}\hat{\varphi}} = -\Gamma^{\hat{\varphi}}{}_{\hat{r}\hat{\varphi}} = -\frac{1}{r}, \qquad \Gamma^{\hat{\theta}}{}_{\hat{\varphi}\hat{\varphi}} = -\Gamma^{\hat{\varphi}}{}_{\hat{\theta}\hat{\varphi}} = -\frac{\cot\theta}{r}. \tag{37}$$

Assuming that the flow is homogeneous with respect to θ and φ, the Enskog equation reads as

$$\begin{aligned}
&\frac{\partial f}{\partial t} + \frac{3p^{\hat{r}}}{m}\frac{\partial(fr^2)}{\partial r^3} + \frac{1}{mr}\left[((p^{\hat{\theta}})^2 + (p^{\hat{\varphi}})^2)\frac{\partial f}{\partial p^{\hat{r}}} - p^{\hat{r}}\left(\frac{\partial(fp^{\hat{\theta}})}{\partial p^{\hat{\theta}}} + \frac{\partial(fp^{\hat{\varphi}})}{\partial p^{\hat{\varphi}}}\right)\right] \\
&\quad = \frac{1}{\tau}(f - f^S) - b\rho\chi f^{\mathrm{MB}}\left\{\xi^r \cdot \left[\partial_r \ln(\rho^2\chi T) + \frac{3}{5}\left(\zeta^2 - \frac{5}{2}\right)\partial_r \ln T\right]\right. \\
&\qquad \left. + \frac{2}{5}\left[2\zeta^{\hat{a}}\zeta^{\hat{b}} : \nabla_{\hat{a}}u^{\hat{b}} + \left(\zeta^2 - \frac{5}{2}\right)\partial_r u^r\right]\right\}.
\end{aligned} \tag{38}$$

The advection term is implemented following Ref. [69].

III. MIXED QUADRATURE LB MODELS

In this paper the mixed quadrature FDLB models are employed, introduced in Refs. [50,51,54,70], to obtain the numerical solution of the Enskog equation in cylindrically and spherically symmetric flows using the simplified Enskog collision operator. These models are briefly described and the reader is encouraged to refer to the above-mentioned references for more details. In the case of the cylindrical Couette flow, the dynamics along the z direction is straightforward. In this context, it is advantageous to integrate out the trivial degrees of freedom in the momentum space at the level of the model equation. The details can be consulted in Ref. [51]. As discussed in Ref. [71], in the Gauss-Hermite quadrature-based models the moments of the

distribution function are recovered up to a certain expansion order N. As such, the resulting evolution of moments up to order N of f is equivalent to that obtained through a Grads expansion procedure. In all Gauss-Hermite quadrature-based models, the set of distribution functions corresponding to the elements of the discrete velocity set is used instead of the moment integrals, resulting in a purely kinetic description of fluid systems.

The velocity sets utilized in these models are determined by Gauss quadrature rules and typically are off lattice, meaning the velocity vectors cannot align simultaneously with neighboring lattice sites. Consequently, the commonly employed collide-and-stream paradigm is unsuitable for these models, necessitating the adoption of finite-difference schemes in this paper to solve the evolution equations. The chosen methods were the third-order total variation diminishing (TVD) Runge-Kutta method for time stepping [72], the fifth-order WENO-5 advection scheme [73,74], and the fourth-order central difference scheme used for gradient evaluation [75].

Another ingredient needed is the evaluation of the average density $\bar{n}$ in Eq. (4). In spherical coordinates one has to evaluate intersections of spherical shells in order to compute the integral in Eq. (4), for which there is an analytic solution. For cylindrical coordinates, one has to rely on numerically computing the intersection between a cylinder shell and a spherical shell. The procedure is detailed in Appendix A.

A. Quadrature choice

Depending on the flow regime under consideration, a mixture of full-range Gauss-Hermite (HLB) and half-range Gauss-Hermite quadratures (HHLB) is considered. Given the choice of the quadrature (full-range or half-range Gauss-Hermite) the total number of quadrature points on the axis a is $\mathcal{Q}_a = Q_a$ or $\mathcal{Q}_a = 2Q_a$, respectively, where Q_a is the quadrature order. In the nonhomogeneous direction (i.e., the radial one) the half-range quadratures are employed and their orders are Q_R and Q_r, in the cylindrical and spherical coordinate systems, respectively. In the homogeneous direction, the full-range quadratures are employed and their orders are Q_φ and (Q_θ, Q_φ). Such a model is denoted [50,51,54]

$$\begin{aligned}\text{Cylindrical}: &\quad \mathrm{HHLB}(N_R; Q_R) \times \mathrm{HLB}(\mathrm{N}_\varphi; \mathrm{Q}_\varphi),\\ \text{Spherical}: &\ \mathrm{HHLB}(N_r; Q_r) \times \mathrm{HLB}(\mathrm{N}_\theta; \mathrm{Q}_\theta) \times \mathrm{HLB}(N_\varphi; Q_\varphi),\end{aligned}$$

where N_a represents the order of the expansion of the equilibrium distribution f^{MB} with respect to axis a, and Q_a is the quadrature order.

The choice of the quadrature controls the momentum-space integration as well as the discretization of the momentum space. In particular, the moments in Eq. (22) are evaluated as

$$\text{Cylindrical}: M^{\hat{a}_1,\ldots,\hat{a}_s} = \sum_{i=1}^{\mathcal{Q}_R}\sum_{j=1}^{\mathcal{Q}_\varphi} f_{ij}\prod_{\ell=1}^{s} p_{ij}^{\hat{a}_\ell}, \tag{39}$$

$$\text{Spherical}: M^{\hat{a}_1,\ldots,\hat{a}_s} = \sum_{i=1}^{\mathcal{Q}_r}\sum_{j=1}^{\mathcal{Q}_\theta}\sum_{k=1}^{\mathcal{Q}_\varphi} f_{ijk}\prod_{\ell=1}^{s} p_{ijk}^{\hat{a}_\ell}. \tag{40}$$

A similar prescription holds for the macroscopic quantities appearing in Eq. (24). In the cylindrical geometry, the discrete momenta components of $\boldsymbol{p}_{ij} = \{p_i^{\hat{R}}, p_j^{\hat{\varphi}}\}$ are indexed on each direction separately, where $1 \leqslant i \leqslant \mathcal{Q}_R$ and $1 \leqslant j \leqslant \mathcal{Q}_\varphi$. In the spherical case, the discrete momenta components of $\boldsymbol{p}_{ijk} = \{p_i^{\hat{r}}, p_j^{\hat{\theta}}, p_k^{\hat{\varphi}}\}$ are indexed as follows: $1 \leqslant i \leqslant \mathcal{Q}_r$, $1 \leqslant j \leqslant \mathcal{Q}_\theta$, and $1 \leqslant k \leqslant \mathcal{Q}_\varphi$. Their components are the roots of the half-range Hermite polynomial $\mathfrak{h}_{Q_a}(x)$ of order Q_a or of the full-range Hermite polynomials $H_{Q_a}(x)$ of order Q_a. Since the roots of the Hermite polynomials are irrational numbers (for full-range Hermite polynomials the roots are rational only for $Q_a < 3$), the ensuing velocity set is off lattice. In the case of the half-range quadrature, the following convention is used: the indices i of the quadrature points lying on the positive semiaxis have the values

$1 \leqslant i \leqslant Q_a$, while the corresponding index of the points on the negative semiaxis have the values $Q_a + 1 \leqslant i \leqslant 2Q_a$ [51].

As an example, for the spherical coordinate system, the link between the Boltzmann distribution function $f(p^{\hat{R}}, p^{\hat{\theta}}, p^{\hat{\varphi}})$ and the discrete distributions f_{ijk} is given through

$$f_{ijk} = \frac{w_i^{\mathfrak{h}}(Q_R) w_j^H(Q_\theta) w_k^H(Q_\varphi)}{\omega\big(p_i^{\hat{R}}\big)\omega\big(p_k^{\hat{\theta}}\big)\omega\big(p_j^{\hat{\varphi}}\big)} f\big(p_i^{\hat{R}}, p_j^{\hat{\theta}}, p_k^{\hat{\varphi}}\big), \tag{41}$$

where $\omega(x) = \frac{1}{\sqrt{2\pi}} e^{-x^2/2}$ is the weight function for the half-range and full-range Hermite polynomials. The quadrature weights for the full-range Gauss-Hermite and half-range Gauss-Hermite polynomials, denoted $w_i^H(Q_a)$ and $w_i^{\mathfrak{h}}(Q_a)$, respectively, are given by

$$w_i^H(Q_a) = \frac{Q_a!}{H_{Q_a+1}^2\big(p_i^{\hat{a}}\big)}, \quad w_i^{\mathfrak{h}}(Q_a) = \frac{p_i^{\hat{a}} a_{Q_a-1}^2}{\mathfrak{h}_{Q_a-1}^2\big(p_i^{\hat{a}}\big)\big[p_i^{\hat{a}} + \mathfrak{h}_{Q_a}^2(0)/\sqrt{2\pi}\big]}, \tag{42}$$

where $a_\ell = \frac{\mathfrak{h}_{\ell+1,\ell+1}}{\mathfrak{h}_{\ell,\ell}}$ is written in terms of the coefficients $\mathfrak{h}_{\ell,s}$ of x^s in the polynomial expansion of $\mathfrak{h}_\ell(x)$ [51].

B. Force terms

The terms involving the derivative of f with respect to momentum vector components require an appropriate treatment since the discretization of the momentum space removes the functional dependence of f on the momentum. Based on the discussion in Refs. [51,54], the two types of force terms are

$$\left(\frac{\partial f}{\partial p^{\hat{a}}}\right)_{ijk} = \sum_{i'=1}^{\mathcal{Q}_a} \mathcal{K}_{i,i'}^a f_{i'jk}, \tag{43}$$

$$\left(\frac{\partial (f p^{\hat{a}})}{\partial p^{\hat{a}}}\right)_{ijk} = \sum_{i'=1}^{\mathcal{Q}_a} \widetilde{\mathcal{K}}_{i,i'}^a f_{i'jk}. \tag{44}$$

The matrix $\mathcal{K}_{i,i'}^a$ in Eq. (43) has the following form:

$$\mathcal{K}_{i,i'}^{a,H} = -w_i^H \sum_{\ell=0}^{Q_a-1} \frac{1}{\ell!} H_{\ell+1}\big(p_i^{\hat{a}}\big) H_\ell\big(p_{i'}^{\hat{a}}\big), \tag{45}$$

$$\mathcal{K}_{i,i'}^{a,\mathfrak{h}} = w_i^{\mathfrak{h}} \sigma_i^{\hat{a}} \left\{ \frac{1 + \sigma_i^{\hat{a}} \sigma_{i'}^{\hat{a}}}{2} \sum_{\ell=0}^{Q_a-2} \mathfrak{h}_\ell\big(\big|p_{i'}^{\hat{a}}\big|\big) \times \left[\frac{\mathfrak{h}_{\ell,0}}{\sqrt{2\pi}} \sum_{s=\ell+1}^{Q_a-1} \mathfrak{h}_{s,0} \mathfrak{h}_s\big(\big|p_i^{\hat{a}}\big|\big) - \frac{\mathfrak{h}_{\ell,\ell}}{\mathfrak{h}_{\ell+1,\ell+1}} \mathfrak{h}_{\ell+1}\big(\big|p_i^{\hat{R}}\big|\big) \right] - \frac{1}{2\sqrt{2\pi}} \Phi_0^{Q_R}\big(\big|p_i^{\hat{R}}\big|\big) \Phi_0^{Q_R}\big(\big|p_{i'}^{\hat{R}}\big|\big) \right\}. \tag{46}$$

for the full-range and half-range quadrature, respectively. In the above, $\sigma_i^{\hat{R}}$ and $\sigma_{i'}^{\hat{R}}$ are the signs of $p_i^{\hat{R}}$ and $p_{i'}^{\hat{R}}$, respectively. The function $\Phi_s^n(x)$ is given by $\Phi_s^n(x) = \sum_{\ell=s}^n \mathfrak{h}_{\ell,s} \mathfrak{h}_\ell(x)$, as defined in Refs. [51,54].

The matrix $\widetilde{\mathcal{K}}^{a}_{i,i'}$ involved in Eq. (44) is written as

$$\widetilde{\mathcal{K}}^{a,H}_{i,i'} = -\,w_i^H \sum_{\ell=0}^{Q_a-2} \frac{1}{\ell!} H_{\ell+1}\big(p_i^{\hat{a}}\big)\big[H_{\ell+1}\big(p_{i'}^{\hat{a}}\big) + \ell H_{\ell-1}\big(p_{i'}^{\hat{a}}\big)\big],$$

$$\widetilde{\mathcal{K}}^{a,\mathfrak{h}}_{i,i'} = -\,w_i^{\mathfrak{h}} \frac{1+\sigma_i^{\hat{a}}\sigma_{i'}^{\hat{a}}}{2} \sum_{\ell=0}^{Q_a-1} \mathfrak{h}_\ell\big(p_i^{\hat{a}}\big)\left[\ell\,\mathfrak{h}_\ell\big(p_{i'}^{\hat{a}}\big) + \frac{\mathfrak{h}^2_{\ell,0}+\mathfrak{h}^2_{\ell-1,0}}{a_{\ell-1}\sqrt{2\pi}}\mathfrak{h}_{\ell-1}\big(p_{j'}^{\hat{a}}\big) + \frac{1}{a_{\ell-1}a_{\ell-2}}\mathfrak{h}_{\ell-2}\big(p_{i'}^{\hat{a}}\big)\right]$$

for the full-range and half-range quadrature, respectively.

C. Equilibrium distribution function

The construction of the equilibrium distribution function (20) follows the prescription developed in Refs. [50,51,70]. f^{MB} is factorized with respect to the momentum space, such that

$$f^{\mathrm{MB}} = n\, g_R(p^{\hat{R}}) g_\varphi(p^{\hat{\varphi}}) g_z(p^{\hat{z}}),$$
$$g_a(p^{\hat{a}}) = \frac{1}{\sqrt{2\pi mT}} \exp\left[-\frac{(p^{\hat{a}}-mu^{\hat{a}})^2}{2mT}\right]. \tag{47}$$

Following the discretization of the momentum space, f^{MB} is replaced by $f^{\mathrm{MB}}_{ijk} = n\, g_{R,i} g_{\varphi,j} g_{z,k}$. The function $g_{a,k}$ becomes [50,51,70]

$$g^H_{a,k} = w_k^H \sum_{\ell=0}^{N_a} H_\ell\big(p_k^{\hat{a}}\big) \sum_{s=0}^{\lfloor \ell/2 \rfloor} \frac{(mT-1)^s (mu^{\hat{a}})^{\ell-2s}}{2^s s!(\ell-2s)!}, \tag{48}$$

$$g^{\mathfrak{h}}_{a,k} = \frac{w_k^{\mathfrak{h}}}{2} \sum_{s=0}^{N_a} \left(\frac{mT}{2}\right)^{s/2} \Phi_s^{N_a}\big(\big|p_k^{\hat{a}}\big|\big) \times \left[(1+\mathrm{erf}\zeta^{\hat{a}})P_s^+(\zeta^{\hat{a}}) + \frac{2}{\sqrt{\pi}} e^{-\zeta_{\hat{a}}^2} P_s^*(\zeta^{\hat{a}})\right], \tag{49}$$

for the case of full-range (superscript H) and half-range (superscript $\mathfrak{h}$) quadrature, respectively. In the above the expansion order N_a is a free parameter satisfying $0 \leqslant N_a < Q_a$. The exact recovery of the moments (21) for polynomials in $p^{\hat{a}}$ of order less than or equal to N_a is ensured by an expansion of $g_{a,k}$ up to order N_a. The expression for $g^{\mathfrak{h}}_{a,k}$ holds the following notations: $\zeta^{\hat{a}} = u^{\hat{a}}\sqrt{m/2T}$ when $p_k^{\hat{a}} > 0$ and $\zeta^{\hat{a}} = -u^{\hat{a}}\sqrt{m/2T}$ when $p_k^{\hat{a}} < 0$, while the polynomials $P_s^+(x)$ and $P_s^*(x)$ are defined as

$$P_s^{\pm}(x) = e^{\mp x^2} \frac{d^s}{dx^s} e^{\pm x^2},$$
$$P_s^*(x) = \sum_{j=0}^{s-1} \binom{s}{j} P_j^+(x) P_{s-j-1}^-(x). \tag{50}$$

IV. NUMERICAL RESULTS

Tests are performed on three distinct setups: the cylindrical Couette and Fourier flows between coaxial cylinders, and the Fourier flow between concentric spheres. The setups are presented in Fig. 1. The inner and outer cylinders and spheres radii are $\mathcal{R}_L \in \{R_L, r_L\}$ and $\mathcal{R}_R \in \{R_R, r_R\}$, respectively, and the diffuse reflection boundary conditions are applied at $\mathcal{R}_L^c = \mathcal{R}_L + \sigma/2$ and $\mathcal{R}_R^c = \mathcal{R}_R - \sigma/2$, which are the limits of the computational domain indicated by the superscript c. The confinement ratio is defined as $C = (\mathcal{R}_R - \mathcal{R}_L)/\sigma = \mathcal{L}/\sigma$, where $\mathcal{L}$ is the physical domain width and $\mathcal{L}^c = \mathcal{L} - \sigma$ is the width of the computational domain. These definitions are depicted graphically in Fig. 2.

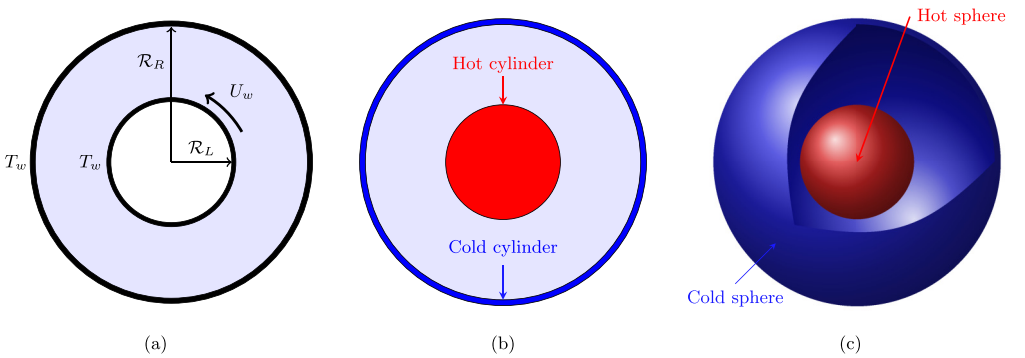

FIG. 1. Setups of the studied problems: (a) cylindrical Couette flow, (b) cylindrical Fourier flow, and (c) spherical Fourier flow.

The FDLB simulation results are validated using a DSMC-like particle method that extends the original direct simulation Monte Carlo (DSMC) method to handle the nonlocal nature of the Enskog collision integral [17]. For a comprehensive explanation of the numerical scheme and an analysis of its computational complexity, please refer to Ref. [26]. The DSMC framework used to solve the Boltzmann equation is maintained, with modifications made to the collision algorithm to accommodate the nonlocal structure of the Enskog collision operator. Following [32], the particle stream is implemented as described in [76] and the collision process takes into account

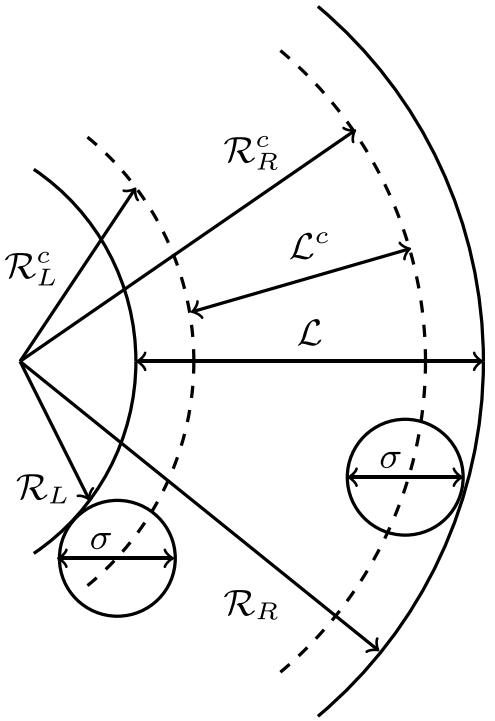

FIG. 2. Radial coordinates used in the paper and the particle diameter σ for context. The dashed lines represent the computational domain, at a distance of $\sigma/2$ from the physical domain.

TABLE I. The Knudsen number Kn for the parameters used in this study.

C		4			7			10	
η_0	0.01	0.1	0.2	0.01	0.1	0.2	0.01	0.1	0.2
Kn	2.8731	0.2261	0.0838	1.64179	0.1292	0.04789	1.1493	0.0904	0.0335

the symmetries of the flow. In this paper, the use of particle variable weights is not mandatory as the computational domain is relatively small, and the numerical scheme associated with variable weights conserves mass, momentum, and energy only in a statistical sense. Using constant weight, the total number of collisions is evaluated in the same manner as in Cartesian coordinates, further simplifying the process. Once a particle is selected, a vector $\hat{\boldsymbol{k}}$ is drawn uniformly from the unit sphere, and the collision partner is chosen at random from the cell corresponding to the radial cell pointed by it. In general, this unit vector identifies a point off the radial axis and, therefore, the velocity components of the selected particle must be rotated to bring its components to be on the radial axis going through that point. The rotations are performed using the rotation matrix associated with the Euler angles. Please refer to [32] for more details. If not stated otherwise, the time step was set to $\Delta t = 10^{-3}$ and the lattice spacing (cell length for particle method) at $\Delta r = \sigma/10$. These values were chosen following a convergence test. A number of $1000V_i/V_0$ (where V_i stands for the volume of the cylindrical and spherical shell) particles per cell was used in the particle method to obtain smooth profiles of macroscopic quantities. The results obtained using this method will be denoted using the abbreviation PM throughout the rest of this paper.

The simulations were conducted for three values of the mean reduced density, $\eta_0 \in \{0.01, 0.1, 0.2\}$, three values of the inner cylinder radius $\mathcal{R}_L \in \{\sigma, 3\sigma, 5\sigma\}$ (corresponding to the computational values $\mathcal{R}_L^c \in \{1.5\sigma, 3.5\sigma, 5.5\sigma\}$), while the outer cylinder radius is $\mathcal{R}_R = \mathcal{R}_L + C\sigma$ [corresponding to the computational value $\mathcal{R}_R^c = \mathcal{R}_L^c + (C-1)\sigma$]. In numerical simulations, three values of the confinement ratio are considered, namely, $C \in \{4, 7, 10\}$, corresponding to $\mathcal{L}_c \in \{3\sigma, 6\sigma, 9\sigma\}$. The values of the associated Knudsen numbers are listed in Table I. The objective is to specifically emphasize the unique characteristics of fluid flow when dense gas effects and confinement are involved. The value of the molecular diameter is fixed at $\sigma = 1$ and, as such, in the following, σ will be dropped when referring to $\mathcal{R}_L$ or $\mathcal{L}_c$. If not stated otherwise, the macroscopic quantities will be plotted with respect to the reduced radius $(\mathcal{R} - \mathcal{R}_L^c)/(\mathcal{R}_R^c - \mathcal{R}_L^c)$.

The typical runtime for a PM simulation in cylindrical coordinates ranges from $\approx 9 \times 10^3$ s for $\eta_0 = 0.01$, $\mathcal{R}_L = 5$ and $C = 4$ to $\approx 8 \times 10^4$ s for $\eta_0 = 0.2$, $\mathcal{R}_L = 1$ and $C = 10$, while in spherical coordinates it ranges from $\approx 1.9 \times 10^4$ s for $\eta_0 = 0.01$, $\mathcal{R}_L = 5$, and $C = 4$ to $\approx 6 \times 10^5$ s for $\eta_0 = 0.2$, $\mathcal{R}_L = 1$, and $C = 10$. For FDLB, at $C = 4$, using a quadrature order of HHLB(7, 20)×HLB(7,8) takes around 700 s, while using HHLB(7, 20)×HLB(7, 8)×HLB(7,8) takes for 2400 s. The running time for FDLB is independent of the reduced density employed but it is directly proportional to the quadrature order and the confinement ratio C (through the number of spatial nodes). This results in a minimum runtime ratio (runtime for PM over the runtime for FDLB) of ≈ 3 for $\eta = 0.01$, $C = 4$, and $\mathcal{R}_L = 5$ in cylindrical Couette flow case [using HHLB(7, 100)×HLB(7,8)] and spherical Fourier flow [using HHLB(7, 60)×HLB(7,8)]. On the other hand, for $\eta_0 = 0.2$, $\mathcal{R}_L = 1$, and $C = 10$ in the spherical Fourier flow case [using HHLB(7, 20)×HLB(7, 8)×HLB(7,8)] one obtains a runtime ratio of ≈ 85. These times were recorded using a single core of an Intel(R) Xeon(R) Gold 6330 CPU running at 2.0 GHz.

Please refer to Appendix C for a comprehensive study of gas at rest between coaxial cylinders and concentric spheres.

A. Cylindrical Couette flow

In this subsection, the cylindrical Couette flow of a gas confined between two infinite coaxial cylinders is analyzed. The inner cylinder rotates about the z axis with fixed velocity $U_w =$

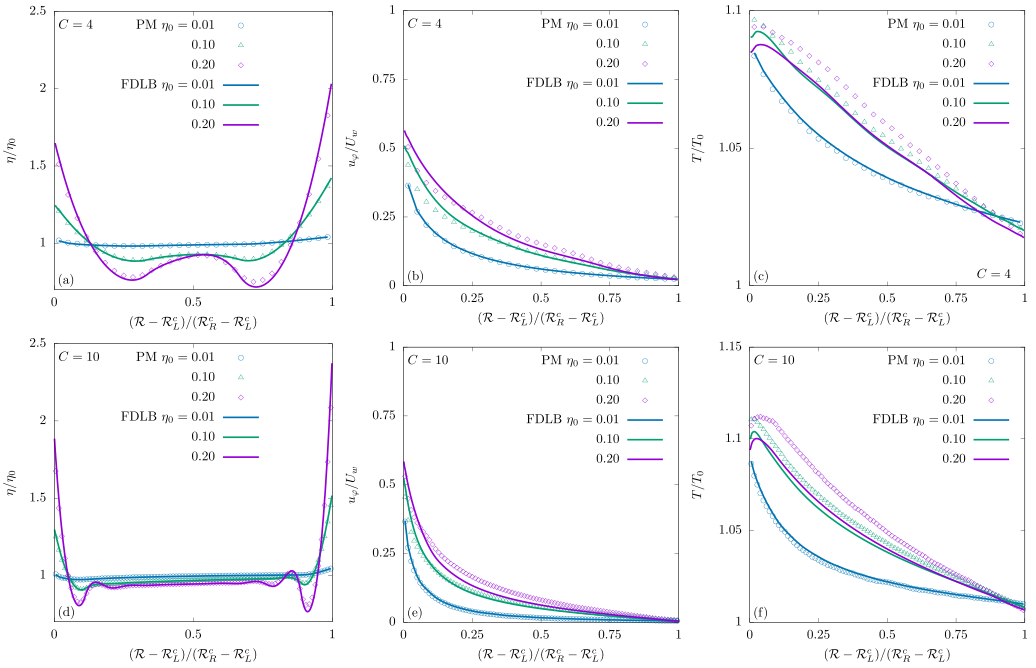

FIG. 3. Cylindrical Couette flow: Normalized (a), (d) reduced density η/η_0, (b), (e) azimuthal velocity u_φ/U_w, and (c), (f) temperature T/T_0, when the inner cylinder radius is $\mathcal{R}_L = 1$, the confinement ratio is $C \in \{4, 10\}$, for three values of the mean reduced density $\eta_0 \in \{0.01, 0.1, 0.2\}$.

$\Omega_w R_L = \sqrt{k_B T_w/m}$, while the outer cylinder is at rest. The wall temperature of both cylinders is equal and constant ($T_w = T_0 = 1$). The simulations were conducted for three values of the mean reduced density $\eta_0 \in \{0.01, 0.1, 0.2\}$, three values of the confinement ratio $C \in \{4, 7, 10\}$, corresponding to $\mathcal{L}_c \in \{3, 6, 9\}$, and three values of the inner cylinder radius $\mathcal{R}_L = \{1, 3, 5\}$ (with the outer cylinder radius $\mathcal{R}_R = \mathcal{R}_L + C$). The corresponding values of the Knudsen number associated with each case are summarized in Table I. The quadratures used in these simulations were HHLB(7, 100)×HLB(7,8) for $\eta_0 = 0.01$ and HHLB(7, 20)×HLB(7,8) for $\eta_0 \in \{0.1, 0.2\}$. Larger values of the quadrature orders do not bring any significant numerical changes to the macroscopic quantities of interest. The expansion order $N = 7$ of the equilibrium distribution function is sufficient to recover the necessary moments for the implementation of the Shakhov relaxation time approximation.

Figures 3(a)–3(c) represent the normalized density η/η_0, azimuthal velocity u_φ/U_w, and temperature T/T_0 for three values of the mean reduced density $\eta_0 \in \{0.01, 0.1, 0.2\}$. The radius of the inner cylinder is $\mathcal{R}_L = 1$ and the confinement ratio was $C = 4$. First, one can observe the influence of the curved boundary on the layering effect near the walls, i.e., the lower value of the reduced fluid density next to the inner cylindrical wall than next to the outer cylinder wall. As explained in Appendix C, when a fluid particle is located at a distance less than σ from the boundary, a portion of its surface remains protected from collisions since there is not enough space available for a second particle to occupy that region. On the other hand, when curved boundaries are considered, this surface shrinks and the space available at a distance σ from the center of the particle increases. It is worth remarking in Fig. 3(a) the nice match between the particle method PM results and the FDLB results for the reduced density profile. Both the azimuthal velocity and the temperature profiles obtained using FDLB are in good agreement with the PM results for small values of η_0. When η_0 is increased, the FDLB results start to depart from the PM results, due to the approximations involved in the simplified Enskog collision operator. Moving to a larger confinement ratio $C = 10$,

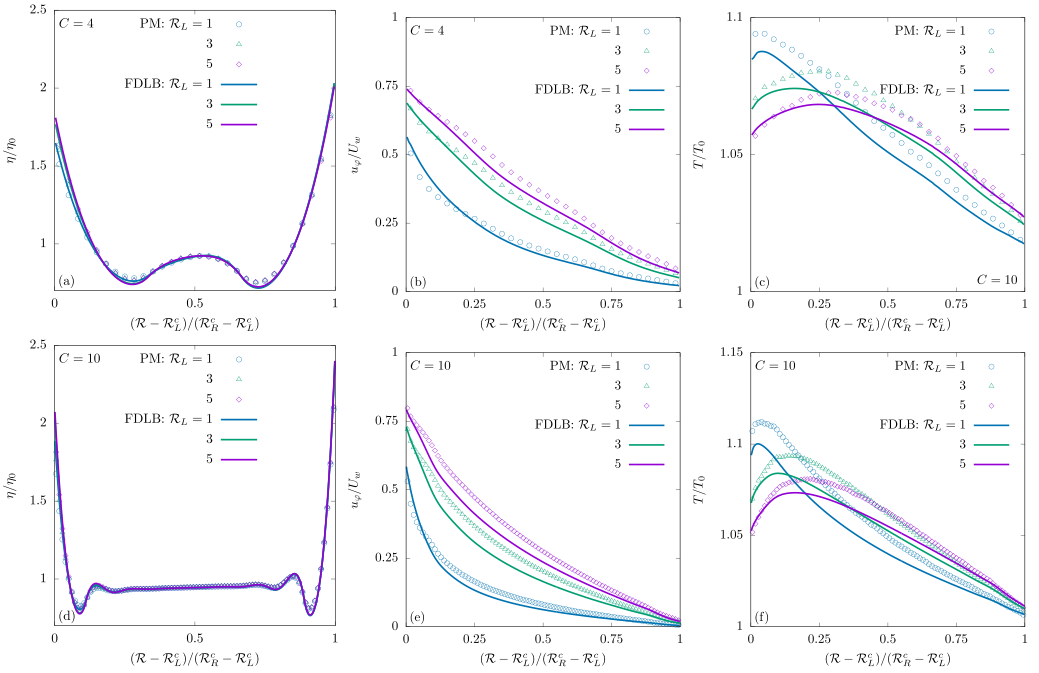

FIG. 4. Cylindrical Couette flow: Normalized (a), (d) reduced density η/η_0, (b), (e) azimuthal velocity u_φ/U_w, and (c), (f) temperature T/T_0 for a mean reduced density of $\eta_0 = 0.2$, two values of the confinement ratio, and three values of the inner cylinder radius $\mathcal{R}_L \in \{1, 3, 5\}$.

one can observe in Figs. 3(d)–3(f) that the layering is more pronounced and the left and right layers are separated (do not interfere). The results show good agreement between FDLB and PM results. The discrepancies in azimuthal velocity are located near the inner cylinder and cover a region of size σ $(1/9\mathcal{L}_c$ in this case), while the FDLB and the PM results temperature profiles are in qualitative agreement and differ only with a relative error of less than 2%–3%.

Next, the focus is on varying the inner cylinder radius $\mathcal{R}_L$. In Fig. 4 are presented the numerical results for the highest mean reduced density $\eta_0 = 0.2$, for a confinement ratio of $C = 4$ in the first row and $C = 10$ in the second row. The columns are dedicated to (from the left) the normalized reduced density η/η_0, the normalized azimuthal velocity u_φ/U_w, and the normalized temperature T/T_0, respectively. One can immediately observe the change in the layering next to the inner cylinder as R_L increases and the curvature diminishes. The FDLB results match very well the PM results even for this high mean reduced density. The azimuthal velocity preserves a discrepancy next to the inner cylinder which is also present in the planar wall case to which these results tend as R_L increases. The temperature has the same qualitative behavior in the FDLB results as the PM results but underestimates them by less than 2%–3%.

Lastly, one can fix the inner cylinder radius at the highest curvature, i.e., $R_L = 1$, and vary the mean reduced density η_0 and the confinement ratio C. Figure 5 presents the comparison of the results obtained using the FDLB and PM methods for $\eta_0 = 0.01$ and 0.2 while varying the confinement ratio $C \in \{4, 7, 10\}$. The first column plots the normalized density and since a reduced coordinate $(\mathcal{R} - \mathcal{R}_L^c)/(\mathcal{R}_R^c - \mathcal{R}_L^c)$ is used the relative size of the particles diminishes and the layering is more pronounced. Excellent agreement is obtained for all values tested. The second and third columns represent the normalized azimuthal velocity and temperature and excellent agreement is obtained for a reduced density of $\eta_0 = 0.01$ as in this case the dense gas effect is small and the results close

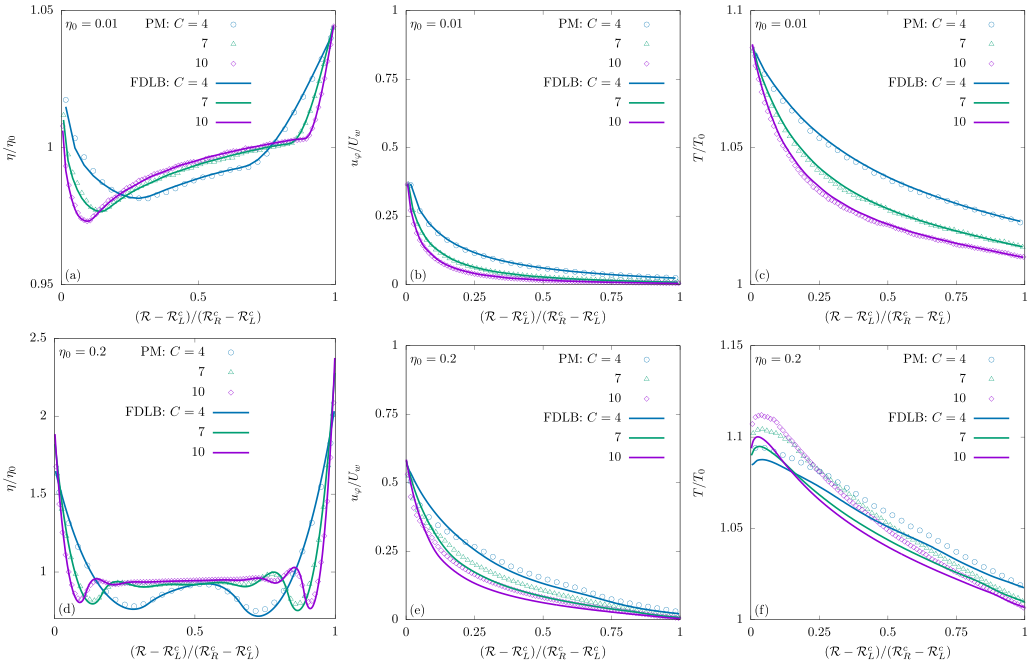

FIG. 5. Cylindrical Couette flow: Normalized (a), (c) reduced density η/η_0, (b), (e) azimuthal velocity u_φ/U_w, and (c), (f) temperature T/T_0 for the inner cylinder radius $\mathcal{R}_L = 1$, two values of the mean reduced density $\eta_0 \in \{0.01, 0.2\}$ and three values of the confinement ratio $C \in \{4, 7, 10\}$.

to the Boltzmann limit are recovered, as in Ref. [51]. For $\eta_0 = 0.2$, a good agreement is obtained overall.

B. Cylindrical and spherical Fourier flows

In this section, the Fourier flow between coaxial cylinders and concentric spheres is studied. The simulations were conducted for three values of the mean reduced density $\eta_0 \in \{0.01, 0.1, 0.2\}$, three values of the confinement ratio $C \in \{4, 7, 10\}$, corresponding to $\mathcal{L}_c \in \{3, 6, 9\}$ and three values of the inner cylinder and sphere radius $\mathcal{R}_L = \{1, 3, 5\}$ (with the outer cylinder and sphere radius of $\mathcal{R}_R = \mathcal{R}_L + C$). The corresponding Knudsen numbers associated with these systems are summarized in Table I. The quadratures used in the cylindrical Fourier flow were HHLB(7, 60)×HLB(7,8) for $\eta_0 = 0.01$ and HHLB(7, 20)×HLB(7,8) for $\eta_0 \in \{0.1, 0.2\}$, while for the spherical case a mixed quadrature of HHLB(7, 60)×HLB(7, 8)×HLB(7,8) for $\eta_0 = 0.01$ and HHLB(7, 20)×HLB(7, 8)×HLB(7,8) for $\eta_0 \in \{0.1, 0.2\}$. Larger values of the quadrature orders do not bring any significant numerical changes to the macroscopic quantities of interest.

1. Cylindrical Fourier flow

Here, the Fourier flow in a gas confined between two infinite coaxial cylinders is analyzed. The inner cylinder temperature is fixed at $T_L = T_0 + \Delta T$ and on the outer cylinder the temperature is $T_R = T_0 - \Delta T$, with $T_0 = 1$, as presented in Fig. 1(b). The results are grouped by varying the mean reduced density η_0 in Fig. 6, the inner cylinder radius $\mathcal{R}_L$ in Fig. 7, and the confinement ratio C in Fig. 8.

As observed in Fig. 6, as the mean reduced density increases the layering is more pronounced in the reduced density plots (top row), while the temperature profile has some discrepancies but is overall in good agreement. As the inner cylinder radius $\mathcal{R}_L$ is increased the reduced density on

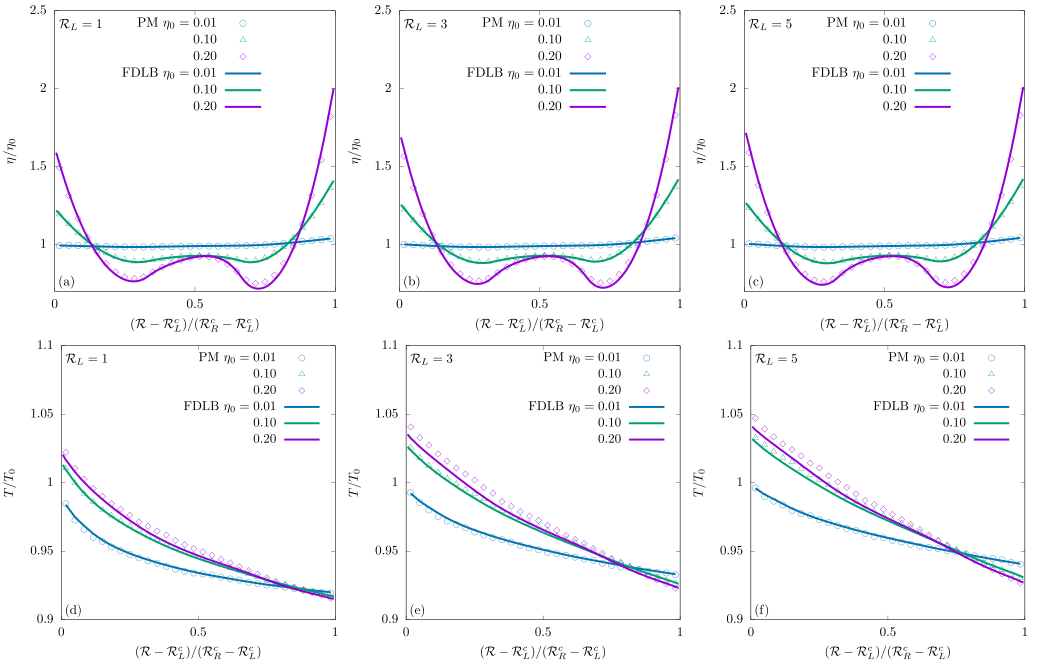

FIG. 6. Cylindrical Fourier flow: Normalized reduced density η/η_0 (a)–(c) and normalized temperature T/T_0 (d)–(f), for $\mathcal{R}_L \in \{1, 3, 5\}$ and the confinement ratio $C = 4$, while lines (FDLB) and points (PM) correspond to varying values of the mean reduced density $\eta_0 \in \{0.01.0.1, 0.2\}$.

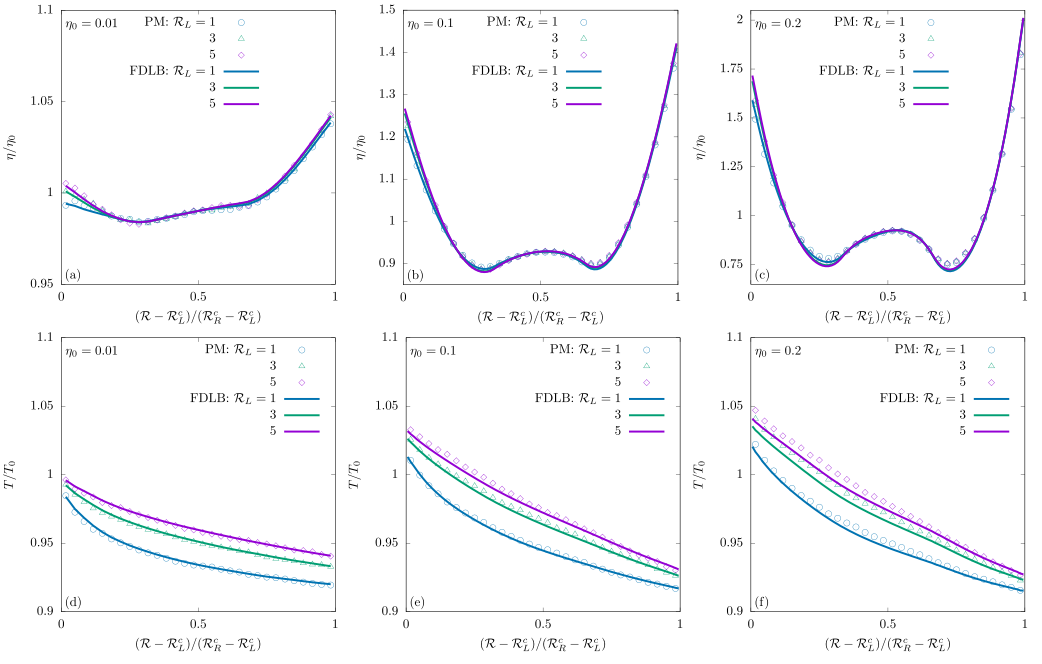

FIG. 7. Cylindrical Fourier flow: Normalized reduced density η/η_0 (a)–(c) and normalized temperature T/T_0 (d)–(f), for $C = 4$ and $\eta_0 \in \{0.01.0.1, 0.2\}$, while the lines (FDLB) and points (PM) correspond to varying values of the inner cylinder radius $\mathcal{R}_L \in \{1, 3, 5\}$.

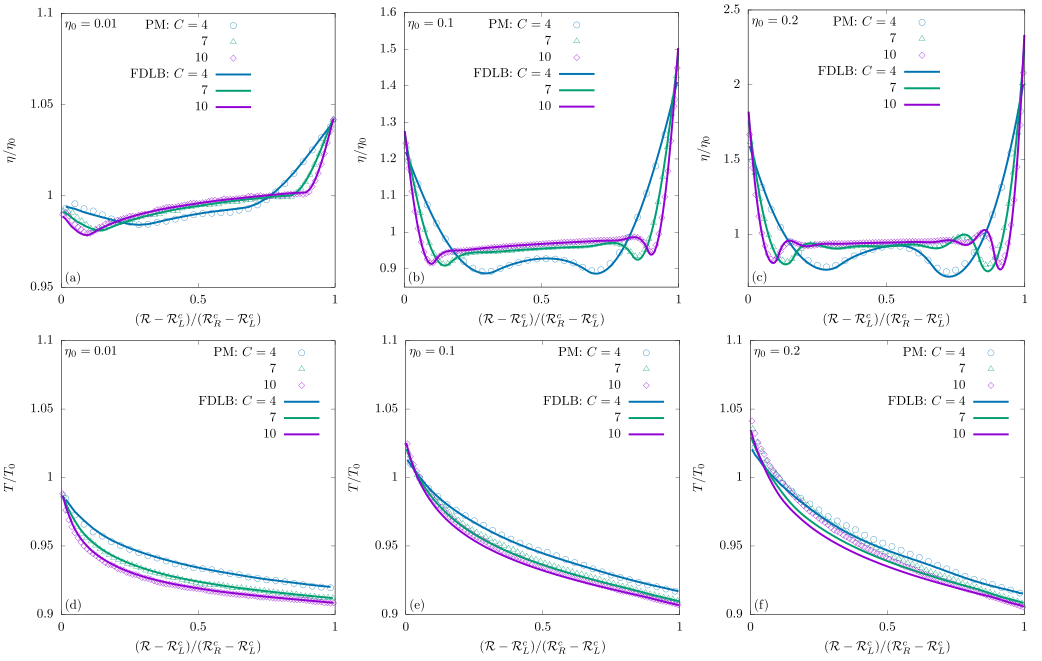

FIG. 8. Cylindrical Fourier flow: Normalized reduced density η/η_0 (a)–(c) and normalized temperature T/T_0 (d)–(f), for $\mathcal{R}_L = 1$ and $\eta_0 \in \{0.01.0.1, 0.2\}$, while the lines (FDLB) and points (PM) correspond to varying values of the confinement ratio $C \in \{4, 7, 10\}$.

the inner cylinder increases as it tends towards the planar wall results [43], and the temperature tends towards a more linear profile as the curvature is diminished. This is more evident in Fig. 7, where the inner radius is varied while keeping the mean reduced density and the confinement ratio fixed. For small η_0 excellent agreement is obtained between the FDLB and PM approaches for both density and temperature, while for the larger values of η_0 the differences in temperature profiles are negligible, at around 2%–3%.

Figure 8 presents the results obtained by varying the confinement ratio C while keeping fixed the mean reduced density η_0 and the inner cylinder radius $\mathcal{R}_L$. The layering in the density profile is changing due to the use of the reduced coordinate $(\mathcal{R} - \mathcal{R}_L^c)/(\mathcal{R}_R^c - \mathcal{R}_L^c)$, such that the relative size of the particle is smaller. Excellent agreement is observed for all values of the confinement ratio at $\eta_0 = 0.01$, while there are some discrepancies at larger values of the mean reduced density, albeit not significant.

2. *Spherical Fourier flow*

In this section, the Fourier flow in a gas confined between two concentric spheres is analyzed. The inner sphere temperature is fixed at $T_L = T_0 + \Delta T$ and on the outer sphere the temperature is $T_R = T_0 - \Delta T$, with $T_0 = 1$, as presented in Fig. 1(c). As in the case of the cylindrical Fourier flow, the results are grouped by varying the mean reduced density η_0 in Fig. 9, the inner sphere radius $\mathcal{R}_L$ in Fig. 10, and the confinement ratio C in Fig. 11.

The results obtained by varying the mean reduced density η_0 and the inner sphere radius $\mathcal{R}_L$ are compiled in Fig. 9. The increase in the mean reduced density leads to a more pronounced layering in the reduced density profiles (top row), while the temperature profile has some discrepancies but is overall in good agreement. As the inner sphere radius $\mathcal{R}_L$ is increased, the reduced density on the inner sphere increases as it tends towards the planar wall results [43], and the temperature tends towards a more linear profile as the curvature is diminished. This is more evident in Fig. 10,

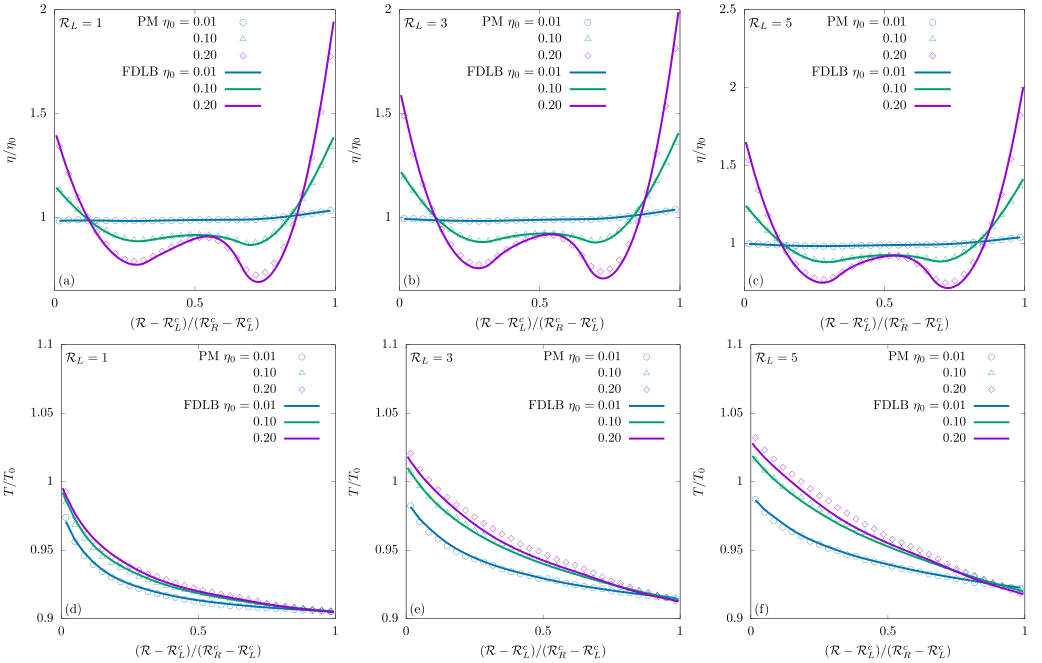

FIG. 9. Spherical Fourier flow: Normalized reduced density η/η_0 (a)-(c) and normalized temperature T/T_0 (d)-(f) for $\mathcal{R}_L \in \{1, 3, 5\}$, and a confinement ratio of $C = 4$, while lines (FDLB) and points (PM) correspond to varying values of the mean reduced density $\eta_0 \in \{0.01.0.1, 0.2\}$.

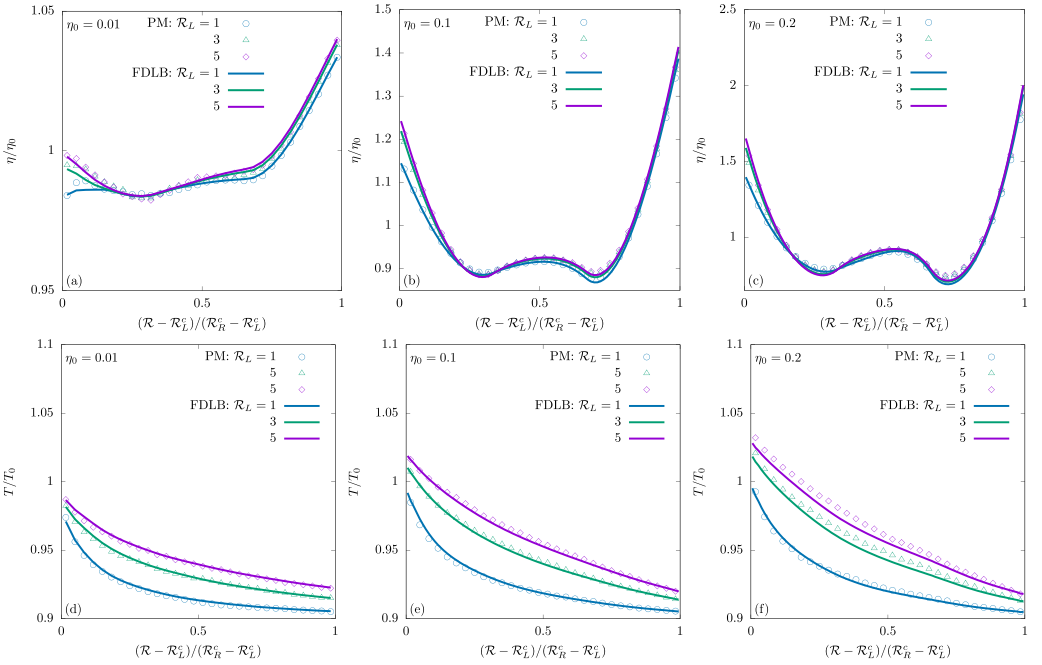

FIG. 10. Spherical Fourier flow: Normalized reduced density η/η_0 (a)-(c) and normalized temperature T/T_0 (d)-(f) for $\eta_0 \in \{0.01.0.1, 0.2\}$, and a confinement ratio of $C = 4$, while the lines (FDLB) and points (PM) correspond to varying values of the inner sphere radius $\mathcal{R}_L \in \{1, 3, 5\}$.

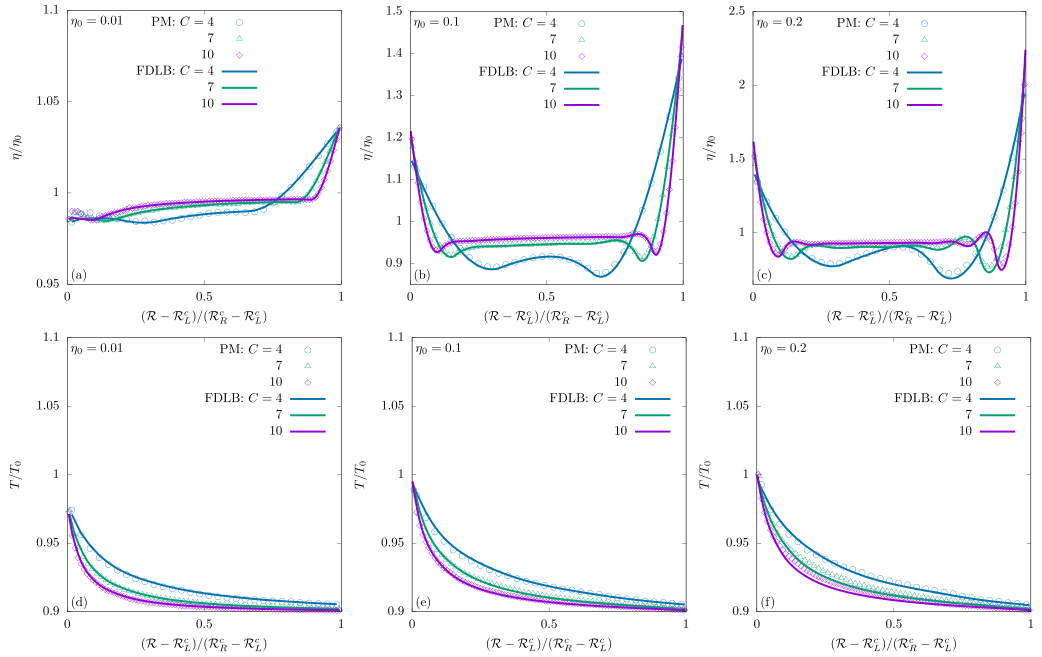

FIG. 11. Spherical Fourier flow: Normalized reduced density η/η_0 (top row) and normalized temperature T/T_0 for $\mathcal{R}_L = 1$ and $\eta_0 \in \{0.01.0.1, 0.2\}$. The lines (FDLB) and points (PM) correspond to varying values of the confinement ratio $C \in \{4, 7, 10\}$.

where the inner radius is varied while keeping the mean reduced density and the confinement ratio fixed. Excellent agreement is obtained between the FDLB and PM approaches for both density and temperature for small mean reduced density η_0, while for the larger values of η_0 the differences in temperature are negligible, at around 2%–3%.

The results obtained by varying the confinement ratio C while keeping fixed the mean reduced density η_0 and the inner sphere radius $\mathcal{R}_L$ are plotted in Fig. 11. As before, due to the use of the reduced coordinate $(\mathcal{R} - \mathcal{R}_L^c)/(\mathcal{R}_R^c - \mathcal{R}_L^c)$ the layering in the reduced density profile is modified since the relative size of the particle is smaller. Excellent agreement is observed for all values of the confinement ratio at $\eta_0 = 0.01$, while there are insignificant discrepancies at larger values of the mean reduced density.

3. Geometry comparisons

In this subsection, the results of the two geometries used in the case of the Fourier flow are directly compared. Figures 12 and 13 present the normalized reduced density η/η_0 (a)–(c) and temperature T/T_0 (d)–(f), when the inner cylinder and sphere radius is $\mathcal{R}_L = 1$, for three values of the mean reduced density $\eta_0 \in \{0.01, 0.1, 0.2\}$ and both geometries considered (cylindrical and spherical), for a confinement ratio of $C = 4$ and 10, respectively. The direct comparison shows the extent to which the variation in the volume excluded by the boundary affects the layering near the wall, especially near the inner cylindrical and spherical boundary, when looking at the reduced density profile. When comparing the temperature profiles one can observe that the spherical profile is always below the cylindrical one. As expected, the results obtained with the FDLB overlap very well with the PM results for low mean reduced density η_0, and have a reasonable accuracy in the temperature profile. One may observe that the agreement in the temperature profile is better in the spherical case. This seems to be related to the lower reduced density on the inner cylinder and sphere, and implicitly lower gradients, as can be seen in the reduced density plots. Since the error

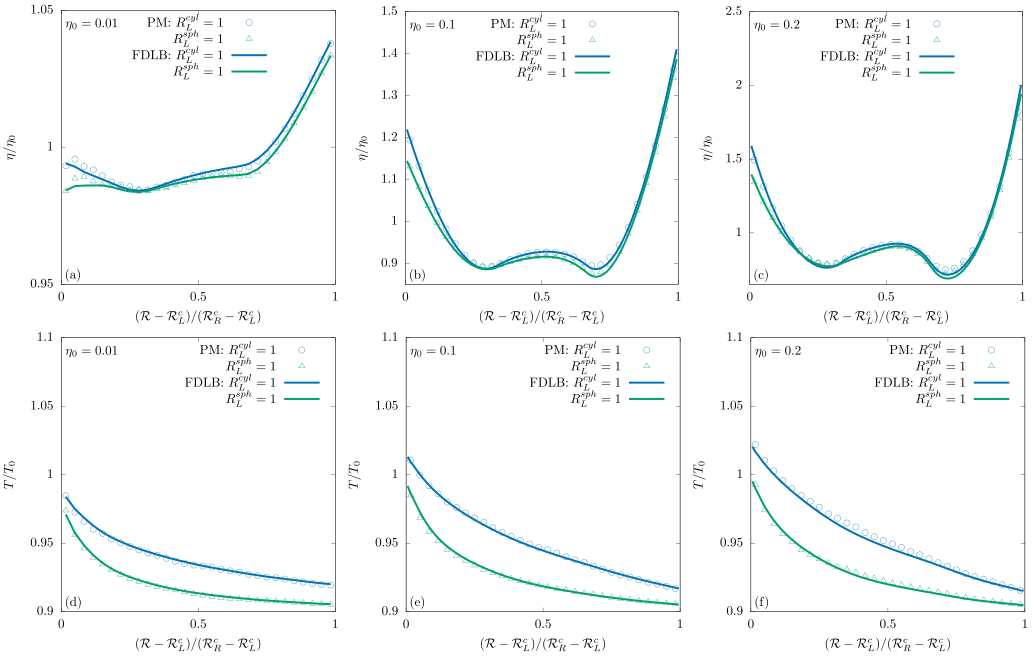

FIG. 12. Fourier flow: Normalized reduced density η/η_0 (a)–(c) and temperature T/T_0 (d)–(f) for the confinement ratio $C = 4$, the inner cylinder and sphere radius $\mathcal{R}_L = 1$, three values of the mean reduced density $\eta_0 \in \{0.01.0.1, 0.2\}$ and the two geometries, cylindrical, and spherical. The variation in the surface of the particle protected from collisions is clearly observed in both reduced density and temperature, with the temperature profile in spherical geometry being always below the cylindrical one.

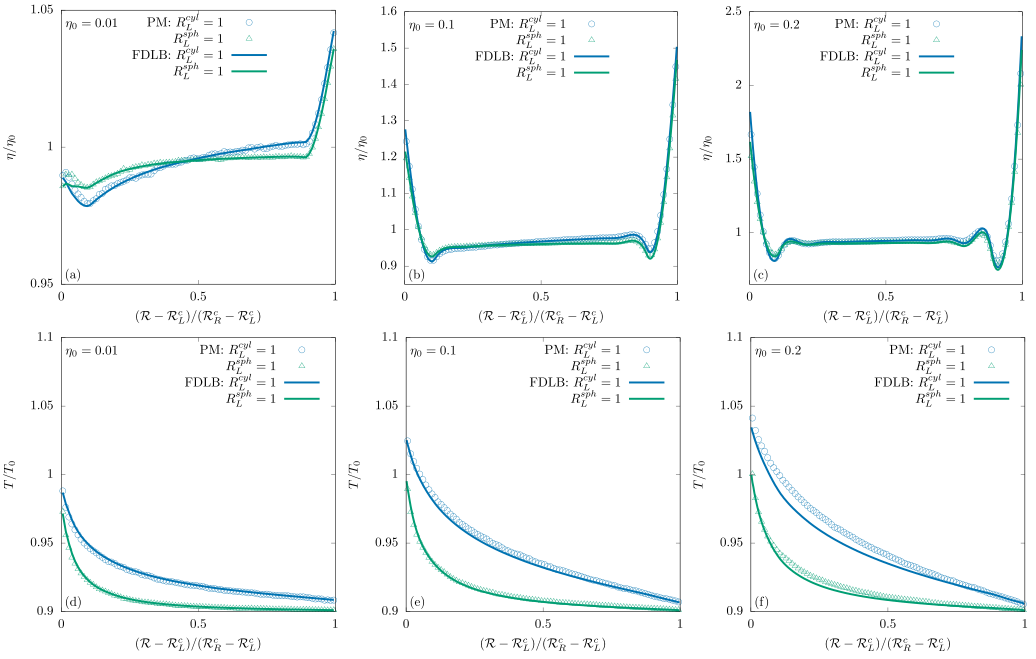

FIG. 13. Fourier flow: Normalized reduced density η/η_0 (a)–(c) and temperature T/T_0 (d)–(f) for the confinement ratio $C = 10$. The rest of parameters are the same as Fig. 12.

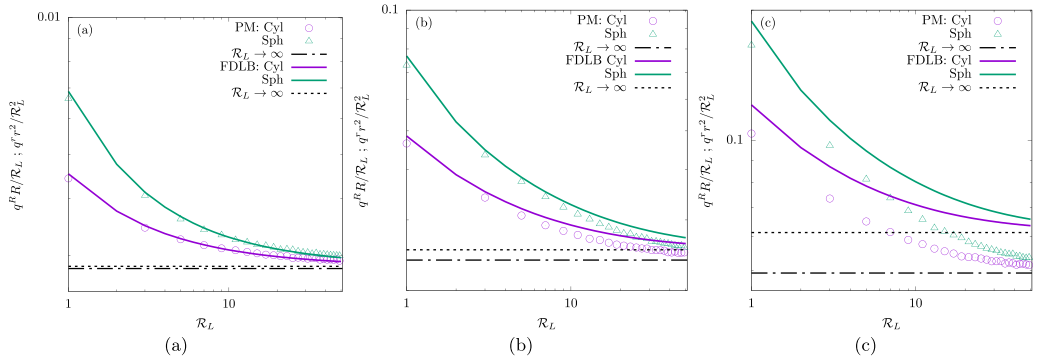

FIG. 14. Fourier flow: The constants $q^R R/\mathcal{R}_L$ and $q^r r^2/\mathcal{R}_L^2$ for a temperature difference of $\Delta T = 0.1$, confinement ratio of $C = 4$, mean reduced density of η_0 of (a) 0.01, (b) 0.1, and (c) 0.2, and variable inner cylinder and sphere radius $\mathcal{R}_L$. As the inner $\mathcal{R}_L$ increases, the two geometries approach a planar wall ($\mathcal{R}_L \to \infty$) and the results tend to match the results obtained in Ref. [43], which are represented as dashed lines.

increases as reduced density increases, the deviations from the PM results increase in the cases when the layering is more pronounced, which agrees with all the results presented.

Furthermore, one can compare the radial heat fluxes obtained in the two geometries. According to the conservation laws, the following quantities are constant through the channel in the cylindrically and spherically symmetric Fourier flows:

$$\text{Cylindrical:} \quad q^R R = \text{const}, \tag{51}$$

$$\text{Spherical:} \quad q^r r^2 = \text{const}. \tag{52}$$

In order to compare these values to the planar case, the following quantities are plotted with respect to the inner cylinder and sphere radius: $q^R R/\mathcal{R}_L$ and $q^r r^2/\mathcal{R}_L^2$. The results are summarized in Fig. 14 for (a) $\eta_0 = 0.01$, (b) $\eta_0 = 0.1$, and (c) $\eta_0 = 0.2$, for both the FLDB and the PM results. The confinement ratio is fixed at $C = 4$ and the inner cylinder and sphere radius is increased from $\mathcal{R}_L = 1$ to 50. At low η_0 an excellent agreement throughout the range of inner cylinder and sphere radius is obtained, while as the mean reduced density is increased the value deviates as was the case for a planar wall, reported in Ref. [43], which is represented in the figures as $\mathcal{R}_L \to \infty$. As observed in the planar case, the FDLB overestimates the PM results quite a lot, but this is expected for higher-order moments since the simplified Enskog collision operator approximation discards the higher-order contributions to the collisional momentum and energy transfer. The simulation results obtained using the PM contain the total heat flux, i.e., the sum of the kinetic and the potential contributions defined in Ref. [43].

V. CONCLUSIONS

In this work, a series of dense gas flows bounded by curvilinear walls were considered in order to validate the proposed finite-difference lattice Boltzmann model employing the simplified Enskog collision integral. For this purpose, the Enskog equation in curvilinear coordinates was written with respect to orthonormal vielbein fields (triads in 3D), by extending the formalism introduced in Ref. [51] for the Boltzmann equation. The vielbein can be used to align the momentum space along the coordinate directions, while also decoupling the dependence of $(\boldsymbol{p} - m\boldsymbol{u})^2$ appearing in the Maxwell-Boltzmann equilibrium distribution on the induced metric tensor. In the simplified Enskog collision model, the Enskog collision integral is approximated using a Taylor expansion and retaining the first-order gradients. Following Ref. [51], a half-range Gauss-Hermite quadrature was used on the axis normal to the curved boundaries studied. The model was benchmarked in

three setups: cylindrical Couette and Fourier flows between coaxial cylinders, as well as the Fourier flow between concentric spheres. The simulation parameters range from a low reduced density value ($\eta_0 = 0.01$) to a relatively high value ($\eta_0 = 0.2$), three values of the inner cylinder radius $\mathcal{R}_L \in \{1, 3, 5\}$, and three values of the confinement ratio $C \in \{4, 7, 10\}$.

The FDLB results obtained for the cylindrical Couette flow and the cylindrical and spherical Fourier flows were validated against the corresponding PM results. Reasonable agreement was observed throughout the parameter range. More specifically, the proposed kinetic model adequately captures the effects of denseness, density inhomogeneity, as well as nonequilibrium phenomena within the range of flow parameters investigated. It is important to consider that when a fluid molecule is located at a distance less than a molecular diameter σ from the wall, a portion of its surface remains protected from collisions since there is not sufficient space available for a second molecule to occupy that part of the spatial domain. As a result, the particle is pushed toward the wall. When dealing with a curved boundary this effect is either diminished or enhanced if a concave or convex boundary is involved. The more pronounced effect is on the inner cylinder and sphere where the available space is increased due to the shape of the boundary. As such, the layering effect is inversely proportional to the curvature. This variation in the layering effect is well captured by the FDLB model proposed.

For the cylindrical Couette flow, the density profile in the channel is recovered with good accuracy, while a reasonable accuracy is observed for the azimuthal velocity and temperature profile, with discrepancies between the FDLB and PM results being lower than 3%. For the Fourier flow, the density and temperature distribution in the channel are presented for all combinations of the input parameters. Good agreement is observed throughout the entire parameter range. A comparison of the two geometries is also included, pointing to their differences and the results which are in accordance with expectations based on the excluded volume for collision due to the variable curvature and geometry. Additionally, a discussion about the heat flux between concentric cylinders and concentric spheres is presented. Channel constants derived from heat flux show larger values for high curvature and reach asymptotically the planar case results as the radius of the cylinders and spheres is increased.

In conclusion, the presented model demonstrates its capability to handle curved geometries for moderately dense gases. Moving forward, the goal is to implement the second-order terms in the Taylor expansion of the Enskog collision integral as well as attractive forces between molecules to address multiphase flows.

ACKNOWLEDGMENTS

This work was supported through a grant from the Ministry of Research, Innovation and Digitization, Project No. PN-III-P1-1.1-PD-2021-0216, within PNCDI III. The author thanks V. Sofonea and V. E. Ambruş for useful discussions regarding this study.

APPENDIX A: VOLUME INTERSECTIONS

In order to evaluate the smoothed density $\bar{n}$ in Eq. (4), in cylindrical coordinates the procedure presented in Ref. [77] is employed. The intersection of the cylinder of radius R and the sphere of radius r is given by

$$V(r,R,b) = \frac{4\pi}{3} r^3 \Theta(R-b) + \frac{4}{3\sqrt{A-C}} \Bigg\{ \Pi(k,-\alpha^2) \frac{B^2 s}{C} + K(k) \left[s(A-2B) + (A-B) \frac{3B-C-2A}{3} \right] + E(k)(A-C) \left(-s + \frac{2A+2C-4B}{3} \right) \Bigg\}, \tag{A1}$$

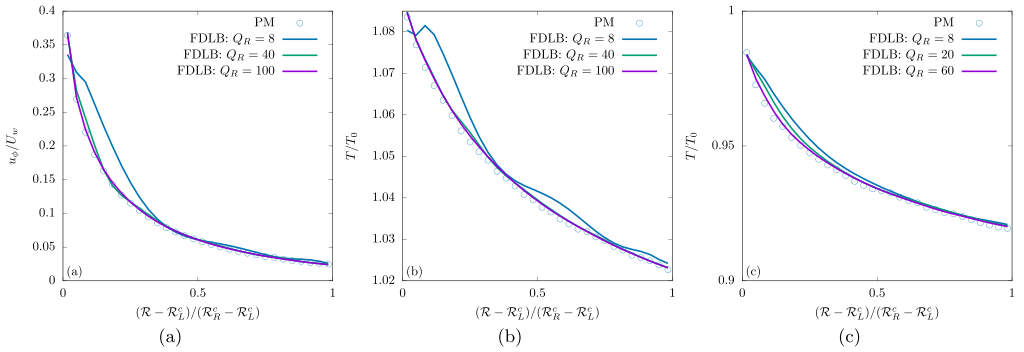

FIG. 15. Comparison of FDLB results obtained in the cylindrical Couette setup for (a) velocity and (b) velocity, with radial quadrature orders of $Q_R \in \{8, 40, 100\}$, and in the setup of the cylindrical Fourier flow for (c) temperature, with radial quadrature orders of $Q_R\{8, 20, 60\}$. The setup is $\mathcal{R}_L = 1$, $C = 4$, and $\eta_0 = 0.01$. This was chosen since it is the most demanding in terms of quadrature order.

for $r < b + R$, where b denotes the smallest perpendicular distance of the axis of the cylinder to the center of the sphere and Θ is the Heaviside step function. The description of the intersection volume is limited to the case used in this study when $r < R$. In the above, the elliptic integrals of the first, second, and third kinds are given by

$$K(k) \equiv \int_0^1 \frac{dz}{\sqrt{1-z^2}\sqrt{1-k^2z^2}}, \quad E(k) \equiv \int_0^1 \frac{dz\sqrt{1-z^2}}{\sqrt{1-k^2z^2}},$$

$$\Pi(k, -\alpha^2) \equiv \int_0^1 \frac{dz}{(1-\alpha^2z^2)\sqrt{1-z^2}\sqrt{1-k^2z^2}} \tag{A2}$$

and the following quantities have been defined:

$$A = \max(r^2, (b+R)^2), \quad B = \min(r^2, (b+R)^2), \quad C = (b-R)^2, \tag{A3}$$

$$k^2 = \frac{B-C}{A-C}, \quad -\alpha^2 = \frac{B-C}{C}, \quad s = (b+R)(b-R). \tag{A4}$$

These expressions were implemented through the use of the GNU Scientific Library (GSL) [78], a numerical library for C and C++ programmers.

In the spherical coordinates, one must evaluate the intersection of two spheres, with radii r_1 and r_2 and the distance between the centers of the spheres of d, for which the analytical expression reads as

$$V(r_1, r_2, d) = \frac{\pi(r_1 + r_2 - d)^2\left(d^2 + 2dr_2 - 3r_2^2 + 2dr_1 + 6r_1r_2 - 3r_1^2\right)}{12d}. \tag{A5}$$

APPENDIX B: QUADRATURE ORDER CONVERGENCE

In this Appendix, the convergence of the FDLB results with respect to the radial quadrature order Q_R in cylindrical coordinates is briefly presented. Figure 15 contains the numerical results obtained using the FDLB model with three values of the radial quadrature, namely, $Q_R \in \{8, 40, 100\}$ for the cylindrical Couette flow and $Q_R\{8, 20, 60\}$ for the cylindrically symmetric Fourier flow. Figures 15(a) and 15(b) contain the velocity and temperature convergence in the cylindrical Couette flow, while Fig. 15(c) shows the convergence of the temperature profile in the cylindrically symmetric Fourier flow. The system parameters are $\mathcal{R}_L = 1, C = 4$, and $\eta_0 = 0.01$, these being the most demanding in terms of quadrature order. One can easily observe the convergence of the FDLB

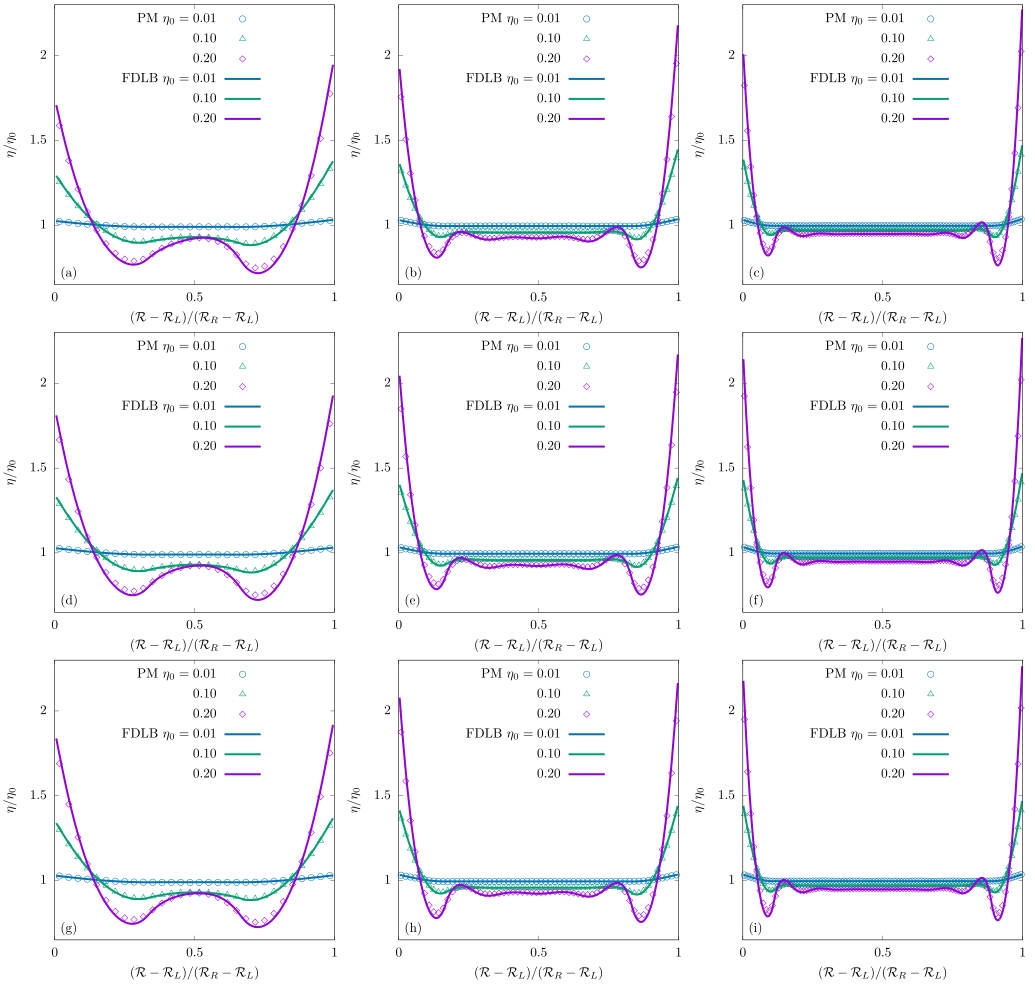

FIG. 16. Gas at rest: Normalized reduced density η/η_0 between coaxial cylinders and three values of the mean reduced density $\eta_0 \in \{0.01, 0.1, 0.2\}$, three values of the inner cylinder radius $\mathcal{R}_L \in \{1, 3, 5\}$ (each row), and three values of the confinement ratio $C \in \{4, 7, 10\}$ (each column).

results and that the quadrature order used in the paper is sufficient. The corresponding results for the spherically symmetric Fourier flow show the same behavior as the cylindrically symmetric Fourier flow.

APPENDIX C: DENSE GAS AT REST BETWEEN COAXIAL CYLINDERS AND CONCENTRIC SPHERES

This Appendix contains the numerical results obtained for a hard-sphere gas at rest confined between two coaxial cylinders and two concentric spheres, kept at the temperature $T_w = 1$. The influence of various system setup variables on the reduced density profile in the channel is analyzed. More specifically, the values chosen are as follows: three values of the mean reduced density $\eta_0 \in \{0.01, 0.1, 0.2\}$, three values of the inner cylinder and sphere radii $\mathcal{R}_L \in \{1, 3, 5\}$, and three values of the channel width, i.e., the distance between cylinders and spheres, denoted using the confinement ratio $C \in \{4, 7, 10\}$, such that the outer cylinder and sphere radius is $\mathcal{R}_R = \mathcal{R}_L + C$.

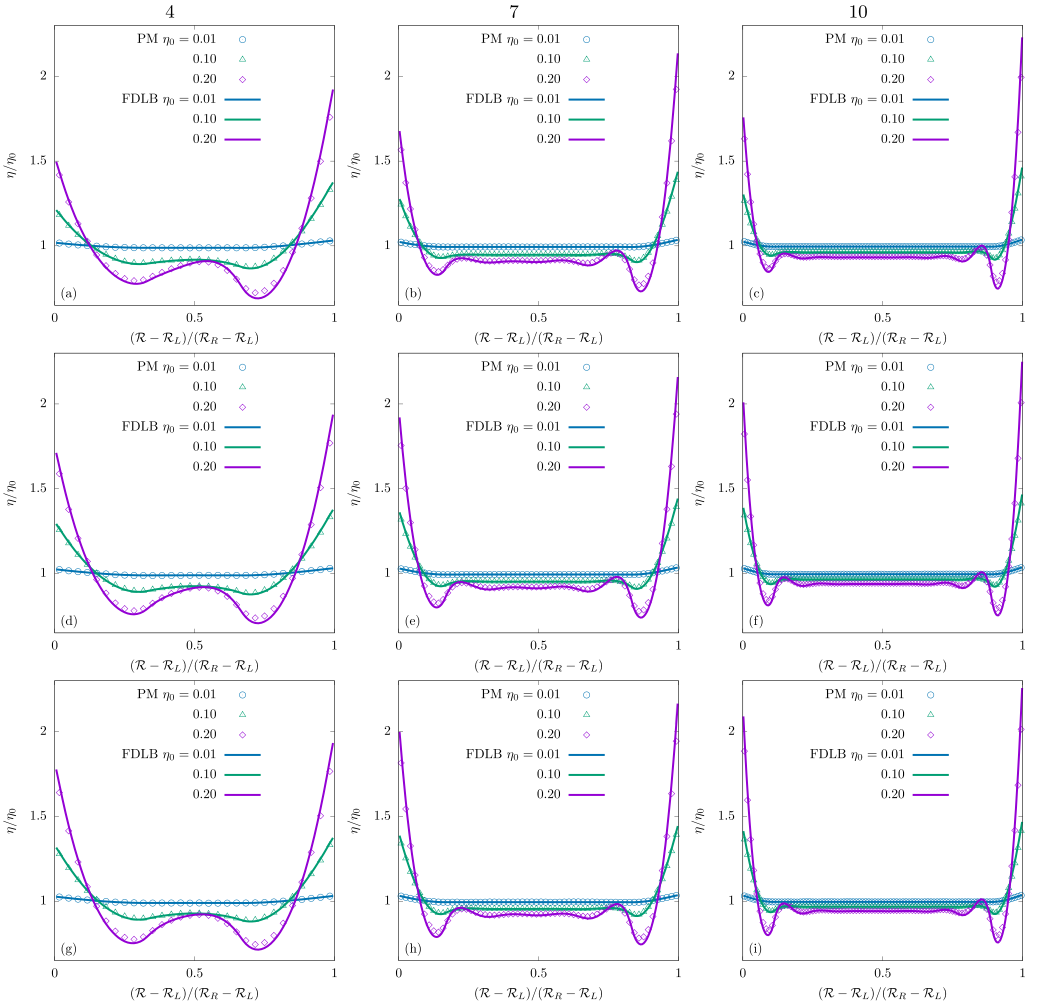

FIG. 17. Gas at rest: Normalized reduced density η/η_0 between concentric spheres and three values of the mean reduced density $\eta_0 \in \{0.01, 0.1, 0.2\}$, three values of the inner cylinder radius $\mathcal{R}_L \in \{1, 3, 5\}$ (each row), and three values of the confinement ratio $C \in \{4, 7, 10\}$ (each column).

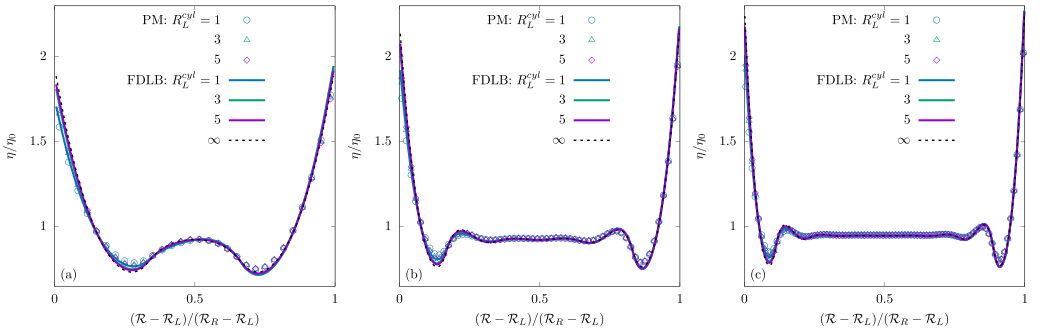

FIG. 18. Gas at rest: Normalized reduced density η/η_0 between coaxial cylinders and three values of the inner cylinder radius $\mathcal{R}_L$, the fixed mean reduced density $\eta_0 = 0.2$, and three values of the confinement ratio $C \in \{4, 7, 10\}$ (a)–(c).

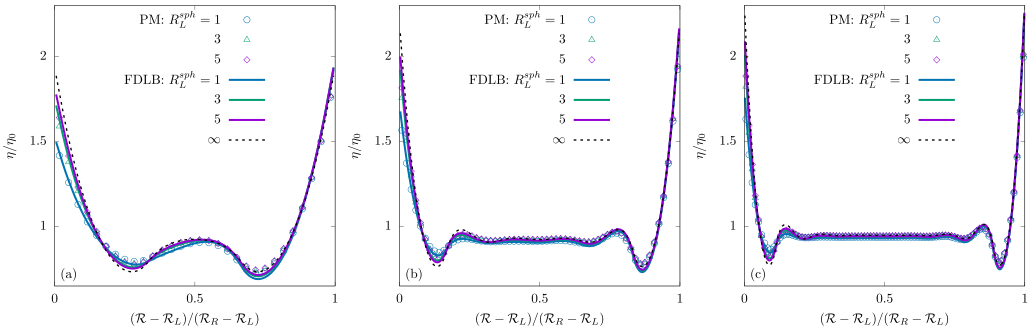

FIG. 19. Gas at rest: Normalized reduced density η/η_0 between concentric spheres, three values of the inner sphere radius $\mathcal{R}_L$, the fixed mean reduced density $\eta_0 = 0.2$, and three values of the confinement ratio $C \in \{4, 7, 10\}$ (a)–(c).

Figures 16 and 17 present the normalized reduced density η/η_0 for a dense gas between coaxial cylinders and concentric spheres, compiled as varying confinement ratio $C \in \{4, 7, 10\}$ along each row and varying inner cylinder radius $\mathcal{R}_L \in \{1, 3, 5\}$ along each column, for three values of the mean reduced density $\eta_0 \in \{0.01, 0.1, 0.2\}$. As was the case for planar wall [43], the stationary profile of the normalized reduced density η/η_0 is nonmonotonic near the wall, a characteristic feature of dense gases, albeit its magnitude depends on the inner cylinder and sphere radius, i.e., the curvature. It is important to consider that when a fluid molecule is located at a distance less than a molecular diameter σ from the wall, a portion of its surface remains protected from collisions since there is not sufficient space available for a second molecule to occupy that part of the spatial domain. As a result, the particle is pushed toward the wall. When dealing with a curved boundary this effect is either diminished or enhanced if a concave or convex boundary is involved. The more pronounced effect is on the inner cylinder and sphere where the available space is increased due to the shape of the boundary. As such the layering effect is inversely proportional to the curvature. Their intensity also diminishes as the dilute gas limit is approached $\eta_0 \to 0$. These density variations emerge within a region approximately equivalent to the molecular diameter σ.

Furthermore, in order to compare to the planar wall limit, plots are made with varying inner radius $\mathcal{R}_L \in \{1, 3, 5\}$, fixed confinement ratio C, and a mean reduced density $\eta_0 = 0.2$, for which the density variations are the largest. The results are displayed in Figs. 18 and 19. One can observe that at a fairly small inner radius of the cylinder, the planar wall $\mathcal{R}_L \to \infty$ result is almost recovered, while for the sphere one needs to go a value larger than $\mathcal{R}_L > 5\sigma$ in order to obtain the overlap.

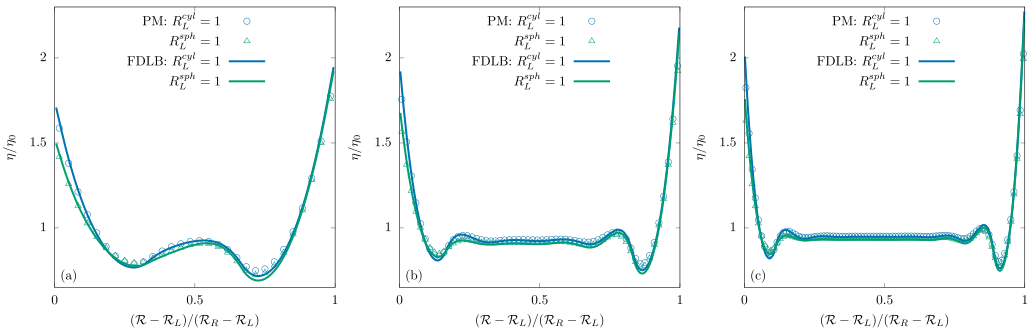

FIG. 20. Gas at rest: Normalized reduced density η/η_0 at $\mathcal{R}_L = 1$ and variable geometry, for fixed mean reduced density $\eta_0 = 0.2$, fixed inner cylinder and sphere radius $\mathcal{R}_L = 1$, and three values of the confinement ratio $C \in \{4, 7, 10\}$ (a)–(c).

Finally, the two geometries are compared to each other for the same parameters. Figure 20 presents the results for $\mathcal{R}_L = 1$, $\eta = 0.2$, and three values of the confinement ratio $C \in \{4, 7, 10\}$. As expected, the layering at the inner wall is smaller in magnitude due to varying collision surfaces.

[1] J. Ferziger and H. Kaper, *Mathematical Theory of Transport Processes in Gases* (North-Holland, Amsterdam, 1972).

[2] M. P. Brenner, S. Hilgenfeldt, and D. Lohse, Single-bubble sonoluminescence, Rev. Mod. Phys. **74**, 425 (2002).

[3] E. L. Petersen and R. K. Hanson, Nonideal effects behind reflected shock waves in a high-pressure shock tube, Shock Waves **10**, 405 (2001).

[4] J. K. Holt, H. G. Park, Y. Wang, M. Stadermann, A. B. Artyukhin, C. P. Grigoropoulos, A. Noy, and O. Bakajin, Fast mass transport through sub-2-nanometer carbon nanotubes, Science **312**, 1034 (2006).

[5] L. Wu, H. Liu, J. M. Reese, and Y. Zhang, Non-equilibrium dynamics of dense gas under tight confinement, J. Fluid Mech. **794**, 252 (2016).

[6] R. Sander, Z. Pan, and L. D. Connell, Laboratory measurement of low permeability unconventional gas reservoir rocks: A review of experimental methods, J. Nat. Gas Sci. Eng. **37**, 248 (2017).

[7] D. Enskog, *Kinetische Theorie der Wärmeleitung: Reibung und Selbst-diffusion in Gewissen verdichteten gasen und flüssigkeiten* (Almqvist & Wiksells, Uppsala, 1922).

[8] S. Chapman and T. G. Cowling, *The Mathematical Theory of Non-uniform Gases: An Account of the Kinetic Theory of Viscosity, Thermal Conduction and Diffusion in Gases* (Cambridge University Press, Cambridge, 1970).

[9] G. M. Kremer, *An Introduction to the Boltzmann Equation and Transport Processes in Gases* (Springer, Berlin, 2010).

[10] J. R. Dorfman, H. van Beijeren, and T. Kirkpatrick, *Contemporary Kinetic Theory of Matter* (Cambridge University Press, Cambridge, 2021).

[11] A. Frezzotti and C. Sgarra, Numerical analysis of a shock-wave solution of the Enskog equation obtained via a Monte Carlo method, J. Stat. Phys. **73**, 193 (1993).

[12] L. Wu, Y. Zhang, and J. M. Reese, Fast spectral solution of the generalized Enskog equation for dense gases, J. Comput. Phys. **303**, 66 (2015).

[13] M. Sadr and M. H. Gorji, A continuous stochastic model for non-equilibrium dense gases, Phys. Fluids **29**, 122007 (2017).

[14] M. Sadr and M. Gorji, Treatment of long-range interactions arising in the Enskog–Vlasov description of dense fluids, J. Comput. Phys. **378**, 129 (2019).

[15] F. J. Alexander, A. L. Garcia, and B. J. Alder, A consistent Boltzmann algorithm, Phys. Rev. Lett. **74**, 5212 (1995).

[16] J. M. Montanero and A. Santos, Monte Carlo simulation method for the Enskog equation, Phys. Rev. E **54**, 438 (1996).

[17] A. Frezzotti, A particle scheme for the numerical solution of the Enskog equation, Phys. Fluids **9**, 1329 (1997).

[18] H. T. Davis, Kinetic theory of inhomogeneous fluid: Tracer diffusion, J. Chem. Phys. **86**, 1474 (1987).

[19] X.-D. Din and E. E. Michaelides, Kinetic theory and molecular dynamics simulations of microscopic flows, Phys. Fluids **9**, 3915 (1997).

[20] A. Frezzotti, Monte Carlo simulation of the heat flow in a dense hard sphere gas, Eur. J. Mech. B Fluids **18**, 103 (1999).

[21] S. Nedea, A. Frijns, A. van Steenhoven, A. Jansen, A. Markvoort, and P. Hilbers, Density distribution for a dense hard-sphere gas in micro/nano-channels: Analytical and simulation results, J. Comput. Phys. **219**, 532 (2006).

[22] Q. Sheng, L. Gibelli, J. Li, M. K. Borg, and Y. Zhang, Dense gas flow simulations in ultra-tight confinement, Phys. Fluids **32**, 092003 (2020).
[23] W. Su, L. Gibelli, J. Li, M. K. Borg, and Y. Zhang, Kinetic modeling of nonequilibrium flow of hard-sphere dense gases, Phys. Rev. Fluids **8**, 013401 (2023).
[24] A. Frezzotti, L. Gibelli, and S. Lorenzani, Mean field kinetic theory description of evaporation of a fluid into vacuum, Phys. Fluids **17**, 012102 (2005).
[25] M. Kon, K. Kobayashi, and M. Watanabe, Method of determining kinetic boundary conditions in net evaporation/condensation, Phys. Fluids **26**, 072003 (2014).
[26] A. Frezzotti, P. Barbante, and L. Gibelli, Direct simulation Monte Carlo applications to liquid-vapor flows, Phys. Fluids **31**, 062103 (2019).
[27] S. Busuioc, L. Gibelli, D. A. Lockerby, and J. E. Sprittles, Velocity distribution function of spontaneously evaporating atoms, Phys. Rev. Fluids **5**, 103401 (2020).
[28] D. Bruno and A. Frezzotti, Dense gas effects in the Rayleigh-Brillouin scattering spectra of SF6, Chem. Phys. Lett. **731**, 136595 (2019).
[29] S. Busuioc and L. Gibelli, Mean-field kinetic theory approach to Langmuir evaporation of polyatomic liquids, Phys. Fluids **32**, 093314 (2020).
[30] K. Kobayashi, K. Sasaki, M. Kon, H. Fujii, and M. Watanabe, Kinetic boundary conditions for vapor–gas binary mixture, Microfluid. Nanofluid. **21**, 53 (2017).
[31] P. Barbante, A. Frezzotti, and L. Gibelli, A kinetic theory description of liquid menisci at the microscale, Kinet. Rel. Models **8**, 235 (2015).
[32] S. Busuioc, A. Frezzotti, and L. Gibelli, A weighted particle scheme for Enskog-Vlasov equation to simulate spherical nano-droplets/bubbles, J. Comput. Phys. **475**, 111873 (2023).
[33] L.-S. Luo, Unified theory of lattice Boltzmann models for nonideal gases, Phys. Rev. Lett. **81**, 1618 (1998).
[34] L.-S. Luo, Theory of the lattice Boltzmann method: Lattice Boltzmann models for nonideal gases, Phys. Rev. E **62**, 4982 (2000).
[35] S. Melchionna and U. M. B. Marconi, Lattice Boltzmann method for inhomogeneous fluids, Europhys. Lett. **81**, 34001 (2008).
[36] X. He and G. Doolen, Thermodynamic foundations of kinetic theory and lattice Boltzmann models for multiphase flows, J. Stat. Phys. **107**, 309 (2002).
[37] T. Chen, L. Wu, L.-P. Wang, and S. Chen, Rarefaction effects in head-on collision of two near-critical droplets, Int. J. Multiphase Flow **164**, 104451 (2023).
[38] P. Wang, L. Wu, M. T. Ho, J. Li, Z.-H. Li, and Y. Zhang, The kinetic Shakhov–Enskog model for non-equilibrium flow of dense gases, J. Fluid Mech. **883**, A48 (2020).
[39] Y.-D. Zhang, A.-G. Xu, J.-J. Qiu, H.-T. Wei, and Z.-H. Wei, Kinetic modeling of multiphase flow based on simplified Enskog equation, Front. Phys. **15**, 62503 (2020).
[40] Y. Gan, A. Xu, H. Lai, W. Li, G. Sun, and S. Succi, Discrete Boltzmann multi-scale modelling of non-equilibrium multiphase flows, J. Fluid Mech. **951**, A8 (2022).
[41] R. Huang, H. Wu, and N. A. Adams, Mesoscopic lattice Boltzmann modeling of the liquid-vapor phase transition, Phys. Rev. Lett. **126**, 244501 (2021).
[42] S. Busuioc, Quadrature-based lattice Boltzmann model for non-equilibrium dense gas flows, Phys. Fluids **35**, 016112 (2023).
[43] S. Busuioc and V. Sofonea, Bounded flows of dense gases, Phys. Rev. Fluids **9**, 023401 (2024).
[44] Z. Guo and T. S. Zhao, Explicit finite-difference lattice boltzmann method for curvilinear coordinates, Phys. Rev. E **67**, 066709 (2003).
[45] Z.-H. Li and H.-X. Zhang, Gas-kinetic numerical studies of three-dimensional complex flows on space-craft re-entry, J. Comput. Phys. **228**, 1116 (2009).
[46] C. Lin, A. Xu, G. Zhang, Y. Li, and S. Succi, Polar-coordinate lattice boltzmann modeling of compressible flows, Phys. Rev. E **89**, 013307 (2014).
[47] M. Watari, Is the lattice boltzmann method applicable to rarefied gas flows? Comprehensive evaluation of the higher-order models, J. Fluids Eng. **138**, 011202 (2016).

[48] K. Hejranfar and M. Hajihassanpour, Chebyshev collocation spectral lattice boltzmann method in generalized curvilinear coordinates, Comput. Fluids **146**, 154 (2017).
[49] A. Velasco, J. Muñoz, and M. Mendoza, Lattice boltzmann model for the simulation of the wave equation in curvilinear coordinates, J. Comput. Phys. **376**, 76 (2019).
[50] V. E. Ambruş and V. Sofonea, Lattice Boltzmann models based on half-range Gauss-Hermite quadratures, J. Comput. Phys. **316**, 760 (2016).
[51] S. Busuioc and V. E. Ambruş, Lattice Boltzmann models based on the vielbein formalism for the simulation of flows in curvilinear geometries, Phys. Rev. E **99**, 033304 (2019).
[52] C. Y. Cardall, E. Endeve, and A. Mezzacappa, Conservative 3 + 1 general relativistic Boltzmann equation, Phys. Rev. D **88**, 023011 (2013).
[53] V. E. Ambruş, S. Busuioc, A. J. Wagner, F. Paillusson, and H. Kusumaatmaja, Multicomponent flow on curved surfaces: A vielbein lattice boltzmann approach, Phys. Rev. E **100**, 063306 (2019).
[54] V. E. Ambrus, V. Sofonea, R. Fournier, and S. Blanco, Implementation of the force term in half-range lattice Boltzmann models, arXiv:1708.03249.
[55] N. F. Carnahan and K. E. Starling, Equation of state for nonattracting rigid spheres, J. Chem. Phys. **51**, 635 (1969).
[56] H. Van Beijeren and M. Ernst, The modified Enskog equation, Physica (Amsterdam) **68**, 437 (1973).
[57] J. Fischer and M. Methfessel, Born-Green-Yvon approach to the local densities of a fluid at interfaces, Phys. Rev. A **22**, 2836 (1980).
[58] E. Shakhov, Generalization of the Krook kinetic relaxation equation, Fluid Dyn. **3**, 95 (1968).
[59] E. Shakhov, Approximate kinetic equations in rarefied gas theory, Fluid Dyn. **3**, 112 (1968).
[60] I. Graur and A. Polikarpov, Comparison of different kinetic models for the heat transfer problem, Heat Mass Transfer **46**, 237 (2009).
[61] V. E. Ambruş, F. Sharipov, and V. Sofonea, Comparison of the Shakhov and ellipsoidal models for the Boltzmann equation and DSMC for *ab initio*-based particle interactions, Comput. Fluids **211**, 104637 (2020).
[62] F. Sharipov, Application of the Cercignani–Lampis scattering kernel to calculations of rarefied gas flows. I. plane flow between two parallel plates, Eur. J. Mech. B Fluids **21**, 113 (2002).
[63] F. Sharipov, Application of the Cercignani–Lampis scattering kernel toÂ calculations of rarefied gas flows. II. slip and jump coefficients, Eur. J. Mech. B Fluids **22**, 133 (2003).
[64] V. E. Ambruş and V. Sofonea, Half-range lattice Boltzmann models for the simulation of Couette flow using the Shakhov collision term, Phys. Rev. E **98**, 063311 (2018).
[65] Y. Zhang, A. Xu, G. Zhang, Z. Chen, and P. Wang, Discrete Boltzmann method for non-equilibrium flows: Based on Shakhov model, Comput. Phys. Commun. **238**, 50 (2019).
[66] B. N. Todorova, C. White, and R. Steijl, Modeling of nitrogen and oxygen gas mixture with a novel diatomic kinetic model, AIP Adv. **10**, 095218 (2020).
[67] B. Shan, W. Su, L. Gibelli, and Y. Zhang, Molecular kinetic modelling of non-equilibrium transport of confined van der waals fluids, J. Fluid Mech. **976**, A7 (2023).
[68] S. A. E. G. Falle and S. S. Komissarov, An upwind numerical scheme for relativistic hydrodynamics with a general equation of state, Mon. Not. R. Astron. Soc. **278**, 586 (1996).
[69] T. P. Downes, P. Duffy, and S. S. Komissarov, Relativistic blast waves and synchrotron emission, Mon. Not. R. Astron. Soc. **332**, 144 (2002).
[70] V. E. Ambruş and V. Sofonea, Application of mixed quadrature lattice Boltzmann models for the simulation of Poiseuille flow at non-negligible values of the Knudsen number, J. Comput. Sci. **17**, 403 (2016).
[71] X. Shan, X.-F. Yuan, and H. Chen, Kinetic theory representation of hydrodynamics: a way beyond the Navier–Stokes equation, J. Fluid Mech. **550**, 413 (2006).
[72] C.-W. Shu and S. Osher, Efficient implementation of essentially non-oscillatory shock-capturing schemes, J. Comput. Phys. **77**, 439 (1988).
[73] Y. Gan, A. Xu, G. Zhang, and Y. Li, Lattice Boltzmann study on Kelvin-Helmholtz instability: Roles of velocity and density gradients, Phys. Rev. E **83**, 056704 (2011).

[74] G.-S. Jiang and C.-W. Shu, Efficient implementation of Weighted ENO schemes, J. Comput. Phys. **126**, 202 (1996).

[75] B. Fornberg, Generation of finite difference formulas on arbitrarily spaced grids, Math. Comput. **51**, 699 (1988).

[76] G. A. Bird, *The DSMC Method* (CreateSpace, US, 2013).

[77] F. Lamarche and C. Leroy, Evaluation of the volume of intersection of a sphere with a cylinder by elliptic integrals, Comput. Phys. Commun. **59**, 359 (1990).

[78] M. Galassi, J. Davies, J. Theiler, B. Gough, G. Jungman, P. Alken, M. Booth, F. Rossi, and R. Ulerich, *GNU Scientific Library Reference Manual*, 3rd ed. (Network Theory LTD, Surrey, UK, 2021).